Journal of Computational Physics **153,** 101–138 (1999)
Article ID jcph.1999.6264, available online at http://www.idealibrary.com on IDEAL®

CASTOR-K: Stability Analysis of Alfvén Eigenmodes in the Presence of Energetic Ions in Tokamaks

Duarte Borba* and Wolfgang Kerner

*Jet Joint Undertaking, Abingdon OX14 3EA, United Kingdom; *Assoc. Euratom/IST Instituto Superior Técnico, Av. Rovisco Pais, 1096 Lisbon, Portugal*
E-mail: dnborba@jet.uk

Received October 27, 1998; revised March 22, 1999

A hybrid magnetohydrodynamic-gyro-kinetic model is developed for the stability analysis of global Alfvén waves in the presence of energetic ions. The ideal MHD model is extended to take into account the perturbed parallel electric field and the finite Larmor radius which are relevant for high temperature plasmas. The gyrokinetic formulation fully includes the tokamak geometry and the effects of non-standard orbits of energetic ions, which experience large excursions away from the magnetic flux surfaces. The algorithms implemented in the CASTOR-K code are presented together with tests of the numerical accuracy. The orbit integration algorithms are optimized. An efficient algorithm is developed for evaluation of the wave-particle energy exchange expressed by the quadratic form δW_{hot}. © 1999 EURATOM

Key Words: controlled fusion; tokamaks; plasma instabilities; magnetohydrodynamics (MHD); Alfvén waves; alpha particles.

I. INTRODUCTION

The excitation of kinetic Alfvén waves by resonant interaction with energetic ions can cause loss of confinement of the fast ions in tokamaks with intense auxiliary heating or in a tokamak fusion reactor [44].

The tokamak geometry yields coupling between different poloidal harmonics of the Alfvén wave, which breaks up the shear Alfvén continuous spectrum and, furthermore, creates discrete global toroidicity-induced shear Alfvén eigenmodes (TAE) with frequencies inside the continuum gaps [7]. In a thermo-nuclear reactor the interaction of alpha particles with the TAEs can lead to instabilities [17]. Unstable TAEs during neutral beam injection were first observed in the TFTR tokamak [50].

Detailed quantitative predictions are required for the accurate analysis of JET D-T discharges and for the design of ITER or other reactor relevant devices. This is beyond the

0021-9991/99 $30.00
Copyright © 1999 by EURATOM
All rights of reproduction in any form reserved.

capability of analytical treatment as done by Kerner *et al*. [30] and Fu and Van Dam [18]. The assessment of the stability of TAEs and kinetic toroidicity-induced eigenmodes (KTAEs) in a fusion reactor needs to be based on realistic plasma equilibria, realistic TAE wave fields, and realistic distribution functions of the energetic ions including finite orbit widths. These requirements prompt the development of a general model which includes all these effects in a self-consistent manner. The influence of the plasma geometry on the TAE and KTAE eigenfunctions is important in analyzing low toroidal mode numbers, where the wavelength is comparable with the plasma dimensions. In particular, toroidal equilibria with non-circular plasma shapes must be considered. In addition, a toroidal model which includes bulk ion finite Larmor radius corrections is required in order to compute the KTAE spectrum. As pointed out by Mett and Mahajan [35], the KTAEs become important in studying the high temperature plasmas characteristic of the present large fusion experiments. The normal-mode MHD code CASTOR [31] has been extended for this purpose. The interaction between the TAE and KTAE wave fields with the energetic particle population has to take into account the finite orbit widths of the high energy ions. The large excursions away from the magnetic flux surfaces experienced by the high energy ions are significant compared with the widths of the relevant TAE and KTAEs. The interaction between the Alfvén waves propagating along the field lines and the energetic ions is significantly reduced due to finite particle orbit effects. In our model, the contribution of large orbits, such as non-standard particle orbits, is included in the stability analysis of both the TAE and KTAE modes using the formalism developed in [42]. Thus, the radial extent of the eigenmode and the radial excursions away from the flux surfaces are computed consistently in toroidal plasmas. This is crucial for the accurate calculation of the energy exchange between the particles and the high-n KTAEs and core localized TAEs. The expressions required for the analysis of JET D-T plasmas and for ITER predictions are derived self-consistently and the corresponding algorithms are developed and programed. Expressions for the particle orbits and orbit topology in straight field line coordinates are obtained. The numerical evaluation of the orbits requires a dedicated algorithm in order to resolve accurately the magnetic axis and the boundaries between different orbit topological regions (e.g., like the trapping-passing boundary). The procedure developed conserves the motion invariants, namely, energy, toroidal canonical momentum, and magnetic momentum, independently of the accuracy of the equilibrium representation. The numerical evaluation of the quadratic form δW_{hot} leads to a six dimensional phase-space integration. The six dimensional phase-space is described using the following variables: energy, magnetic momentum, poloidal angle, and cyclotronic phase, together with the toroidal canonical momentum and toroidal angle. Both numerical and analytical methods are employed in each step of the integration. The final integration step with respect to magnetic momentum and toroidal canonical momentum is performed numerically using a two dimensional adaptive scheme. The procedure works in two phases. At first, a rectangular mesh is constructed evaluating the function to be integrated at each point. Thus, a first estimate of the integral is obtained. Second, a refinement criterion selects the area where accumulation points are required for improvement in the accuracy of the integration. This procedure is repeated until a predefined accuracy of the integration is achieved. This numerical procedure is implemented in the new code CASTOR-K.

The paper is organized as follows: In Section II, a general formulation for the study of the excitation of Alfvén eigenmodes by energetic ions in tokamaks is derived. A quadratic form δW_{hot} is constructed which measures the effect of the energetic particles on the stability of global Alfvén modes. The emphasis is placed on the importance of the finite excursions of

the energetic particles away from the flux surfaces leading to a detailed description of the particle orbits. Therefore, the equations of motion are formulated in a specific flux coordinate system, leading to a complete characterization of the orbit topology of high energy ions. In Section III, a group of numerical codes is presented. The introduction of a generalized form for the plasma resistivity in the linear resistive MHD code CASTOR is described. The numerical evaluation of the quadratic form δW_{hot}, which represents the energy exchange between the Alfvén eigenmodes and the energetic particles, is performed by the CASTOR-K code. The different steps of the integration procedure are presented in detail. Appropriate numerical algorithms for the large scale numerical evaluation are developed and tested. Conclusions are contained in Section IV. Details of the particle motion in straight field line coordinates are given in Appendixes 1 and 2. Appendix 3 is devoted to the accuracy of the field line representation.

II. THE MODEL

The stability analysis of a plasma configuration is performed by means of an hybrid model. The fluid part of the model solves the linearized resitive MHD equations,

$$\omega\delta\rho = -\nabla\cdot(\rho_0\delta\vec{v}) \tag{II.1}$$

$$\omega\rho_0\delta\vec{v} = -\nabla\cdot(\rho_0\delta\mathrm{T}+\delta\rho\mathrm{T}_0)+(\nabla\times\vec{B}_0)\times(\nabla\times\delta\vec{A})-\vec{B}_0\times(\nabla\times\nabla\times\delta\vec{A}) \tag{II.2}$$

$$\omega\rho_0\delta P = -\rho_0\delta\vec{v}\cdot\nabla p_0-(\gamma_p-1)p_0\nabla\cdot\delta\vec{v}+2\eta(\gamma-1)(\nabla\times\vec{B}_0)\cdot(\nabla\times\nabla\times\delta\vec{A}) \tag{II.3}$$

$$\omega\,\delta\vec{A} = -\vec{B}_0\times\delta\vec{v}-\eta\nabla\times\nabla\times\delta\vec{A}, \tag{II.4}$$

where $\delta\rho$ represents the plasma density perturbation, $\delta\vec{v}$ the perturbed fluid velocity, δP the perturbed pressure, $\delta\vec{A}$ the perturbed vector potential, η the plasma resistivity, γ_p the adiabatic plasma compressibility constant, p_0 the equilibrium plasma pressure, B_0 the equilibrium magnetic field, and ω the eigenvalue.

The gyro-kinetic part includes the interaction of the energetic ions with the MHD wave using a perturbative approach. The evolution of the particle distribution function f_p in the presence of electromagnetic fields is described by the collisionless Vlasov equation. Using the position of the guiding center $\vec{R}$, the parallel velocity $v_\parallel$, the perpendicular velocity, and the gyro-angle α as variables the Vlasov equation has the form

$$\frac{\partial f_p}{\partial t}+\dot{\vec{R}}\cdot\nabla f_p+\dot{v}_\parallel\frac{\partial f_p}{\partial v_\parallel}+\dot{v}_\perp\frac{\partial f_p}{\partial v_\perp}+\dot{\alpha}\frac{\partial f_p}{\partial\alpha}=0. \tag{II.5}$$

In the usual gyro-kinetic approximation, where the cyclotronic motion of the particle around the magnetic field line is averaged in time, the dimensions of the system are reduced from six to five. This allows the study of time scales which are large compared to the cyclotronic motion, thus the fast varying term $\dot{\alpha}(\partial f_p/\partial\alpha)$ is eliminated in the Vlasov equation by the averaging procedure. The solution of the time dependent Vlasov equation is obtained perturbatively. The zeroth order solution, the time independent solution, is obtained for a distribution of particles in a time independent electromagnetic field (E_0, B_0) in the form of the single particle constants of motion. A steady-state distribution of particles in a toroidally symmetric magnetic field is given by a function of energy E, canonical toroidal momentum P_ϕ, and the magnetic momentum μ. The dependence on $\sigma = \in\{-1, 1\}$ is due to the fact that for a given (E, P_ϕ, μ) there can exist zero, one, or two orbits. In the case where two

orbits exist, the sign of σ will distinguish these two orbits. In the case of large non-standard orbits, σ can be chosen as the time derivative of the toroidal angle $\sigma = \text{sign}(\dot{\phi})$. For orbits with a very small excursion from the poloidal flux surfaces, σ can also be identified with the sign of $v_\parallel$ or $\dot{\theta}$. In the presence of a perturbed time dependent electromagnetic field, $(E(t), B(t)) = (E_0, B_0) + (E_1(t), B_1(t))$, the corresponding linear perturbed distribution function f_1 (i.e., $f_p = F_0 + f_1$) is obtained from the linearized perturbed Vlasov equation

$$\frac{df_1}{dt} = -\dot{v}_\parallel^{(1)} \frac{\partial F_0}{\partial v_\parallel} - \dot{v}_\perp^{(1)} \frac{\partial F_0}{\partial v_\perp}. \tag{II.6}$$

Therefore, the total perturbed distribution function is

$$f_1 = \Phi^{(1)} \frac{\partial F_0}{\partial E} + P_\phi{}^{(1)} \frac{\partial F_0}{\partial P_\phi} - \mu \frac{B^{(1)}}{B} \frac{\partial F_0}{\partial \mu} + h_1, \tag{II.7}$$

$$\frac{dh_1}{dt} = \frac{\partial F_0}{\partial E} \frac{\partial L}{\partial t}^{(1)} - \frac{\partial F_0}{\partial P_\phi} \frac{\partial L}{\partial \phi}^{(1)}, \tag{II.8}$$

where the linearized perturbed Lagrangian $L^{(1)}$ of the unperturbed particle motion up to first order in $O(\frac{1}{\Omega})$ is given by

$$L^{(1)} = Ze\left(\vec{A}^{(1)} + \frac{1}{\Omega} v_\parallel \vec{b}^{(1)}\right) \cdot \dot{\vec{R}} - \Phi^{(1)} - \mu B^{(1)}. \tag{II.9}$$

$\vec{R}$ is the particle position, $v_\parallel$ is the particle velocity parallel to the magnetic field, $\vec{A}^{(1)}$ is the perturbed vector potential, $\Phi^{(1)}$ is the perturbed electrostatic potential, and μ is the particle magnetic moment.

Expressions (II.7)–(II.8) indicate that the total perturbed distribution function can be expressed in terms of the sum of the non-adiabatic part h_1 and the adiabatic contribution. The fact that the orbit motion is periodic is used in the integration of Eq. (II.8).

In this analysis the plasma is described by two classes of particles. The low energy particles which contain most of the plasma pressure are described as a conducting magnetized fluid, i.e., by the MHD model, while the energetic particles have to be treated by a gyro-kinetic approach. The plasma dispersion relation in the ideal MHD framework can be written in the self-adjoint quadratic form

$$\omega^2 E_k = \delta W_{MHD}, \tag{II.10}$$

where E_k is the kinetic energy of the perturbation and δW_{MHD} is the potential energy. With the inclusion of the fast particles the system is no longer self-adjoint. But in the case where the contribution of the hot particles is small $\delta W_{\text{Hot}} \ll \delta W_{MHD}$, the problem can be treated perturbatively. In zeroth order, the normal mode problem is solved in the ideal MHD framework as a generalized eigenvalue problem. The first order correction to the eigenvalue, due to the presence of the additional supra-thermal particle population, is computed using the eigenvectors obtained for each MHD eigenvalue. This first order approximation neglects the fast particle contribution to the eigenfunction but gives the leading order estimate of the growth rate of the MHD wave ω_i. Therefore, the growth rate of a marginally stable wave is given by

$$(\omega_r + i\omega_i)^2 E_k = \delta W_{MHD} + \delta W_{\text{hot}}, \tag{II.11}$$

$$\frac{\gamma}{\omega} = \frac{\omega_i}{\omega_r} = \frac{\text{Im}[\delta W_{\text{hot}}]}{2\omega_r^2 E_k}. \tag{II.12}$$

It is required to compute $\mathrm{Im}[\delta W_{\mathrm{hot}}]$ for a given fast particle distribution F_0. δW_{hot} can be obtained from the perturbed distribution f_1.

Since only the non-adiabatic part of f_1 can give an imaginary contribution to the dispersion function a quadratic form including a supra-thermal particle distribution is obtained [42],

$$\delta W_{\mathrm{hot}} = -\frac{2\pi^2}{Zem^2} \sum_{\sigma} \int dP_\phi \, dE \, d\mu \sum_{\tilde{p}=-\infty}^{\infty} \tau_b(\omega - n\omega_*) \frac{\partial F}{\partial E} \frac{|Y_{\tilde{p}}|^2}{\omega + n\omega_D + (nq + \tilde{p})\omega_b}. \tag{II.13}$$

The perturbed Lagrangian is bounce averaged over the particle orbits and expanded in Fourier harmonics of the periodic particle motion

$$L^{(1)} = \hat{L}^{(1)} e^{-in\phi(\tau)}, \tag{II.14}$$

with n the toroidal wave number. The Fourier coefficients are defined as

$$Y_{\tilde{p}} = \oint \frac{d\tau}{\tau_b} \tilde{L}^{(1)} e^{i\tilde{p}\omega_b \tau}. \tag{II.15}$$

The denominator in the δW_{hot} expression vanishes if

$$\Gamma(E) = \omega + n\omega_D + (nq + \tilde{p})\omega_b = 0; \tag{II.16}$$

this implies that the particle is in resonance with the wave. Taking into account the singularities of the integrand, the integral has to be performed over the phase space. The term proportional to ω represents the free energy due to the gradients in velocity space, causing the Landau damping, while the term proportional to $n\omega_*$ represents the free energy available due to the spatial gradients in the distribution function

$$\omega_* = \frac{\partial F / \partial P_\phi}{\partial F / \partial E}. \tag{II.17}$$

In the evaluation of the growth rate it is necessary to compute the imaginary part of δW_{hot}. Since only the poles in the particle wave response can give an imaginary contribution to δW_{hot}, the three, dimensional integral is reduced to two dimensions by integrating along the resonant condition $\Gamma(E) = 0$. In the evaluation of the growth rate the δW_{hot} quadratic form is reduced to

$$\delta W_{\mathrm{hot}} = -\frac{2\pi^2}{\Omega m^2} \int dP_\phi \, d\mu \sum_{\sigma} \sum_{\tilde{p}=-\infty}^{\infty} \tau_b(\omega - n\omega_*) \frac{\partial F}{\partial E} \frac{2\pi i |Y_{\tilde{p}}|^2}{|\partial \Gamma / \partial E|}. \tag{II.18}$$

II.1. *Particle Orbits and Orbit Topology*

The gyro-averaged guiding centre equations of motion are obtained from a variational principle where the Lagrangian is

$$L = Ze\left(\vec{A} + \frac{1}{\Omega} v_\parallel \vec{B}\right) \cdot \dot{\vec{R}} + \frac{1}{\Omega} \mu B \dot{\Theta} - H, \tag{II.1.1}$$

and

$$H = \frac{1}{2} m v_\parallel^2 + \mu B + Ze\Phi. \tag{II.1.2}$$

$\vec{R}$ is the particle position, $v_\parallel$ is the particle velocity parallel to the magnetic field, $\vec{A}$ is the vector potential, Φ is the electrostatic potential, μ is the particle magnetic moment, Θ is the gyro-angle, and Ω the gyro-frequency. From the Euler–Lagrange equations the following guiding center equations of motion are obtained [33],

$$\left(B + \frac{v_\parallel}{\Omega}\vec{B}\cdot(\nabla\times\vec{b})\right)\dot{\vec{R}} = v_\parallel\vec{B} + \frac{v_\parallel^2 B}{\Omega}\nabla\times\vec{b} + \frac{\mu B}{m\Omega}\vec{b}\times\nabla B, \tag{II.1.3}$$

$$\left(B + \frac{v_\parallel}{\Omega}\vec{B}\cdot(\nabla\times\vec{b})\right)\dot{v}_\parallel = -\frac{\mu}{m}\vec{B}\cdot\nabla B - \frac{v_\parallel\mu B}{m\Omega}(\nabla\times\vec{b})\cdot\nabla B. \tag{II.1.4}$$

These equations describe the guiding centre particle motion up to first order in the Larmor radius but the energy E and canonical angular momentum P_ϕ are exactly conserved in time independent and toroidally symmetric magnetic fields

$$E = \frac{1}{2}mv_\parallel^2 + \mu B + Ze\Phi, \tag{II.1.5}$$

$$P_\phi = Ze\psi + \frac{ZeR}{\Omega}v_\parallel B_\phi, \tag{II.1.6}$$

where B_ϕ denotes the toroidal magnetic field and ψ is the poloidal magnetic flux.

General toroidal configurations are analyzed using specific toroidal magnetic flux coordinates (called CASTOR coordinates). The CASTOR flux coordinates are defined by the radial coordinate $s = \sqrt{\psi/\psi_1}$, the poloidal angle $\tilde{\theta}$, and the toroidal angle ϕ. ψ is the poloidal magnetic flux at a given flux surface and ψ_1 the total poloidal flux. ϕ is the usual toroidal angle but $\tilde{\theta}$ is chosen such that the magnetic field lines are straight in the $(\tilde{\theta},\phi)$ plane, $\frac{d\phi}{d\tilde{\theta}} = q(s)$. It is possible to construct a non-orthogonal coordinate system using the fact that

$$B = \nabla\phi\times\nabla\psi + F\nabla\phi, \tag{II.1.7}$$

with contra-variant components

$$B^3 = \frac{F}{R^2}, \tag{II.1.8}$$

$$B^2 = \frac{f}{J}, \tag{II.1.9}$$

$$\frac{B^3}{B^2} = q(s). \tag{II.1.10}$$

J is the Jacobian of the coordinate system $(s,\tilde{\theta},\phi)$ and $f(s)\nabla s = \nabla\psi$ (see Appendix 1). Thus, the particle guiding center equations of motion take the form (see Appendix 2)

$$\left(1 - \frac{1}{\Omega}v_\parallel\Theta_7\right)\dot{s} = v_\parallel\Theta_1^1 + \frac{v_\parallel^2}{\Omega}\left(\Theta_2^1 + \Theta_1^1\Theta_7\right) + \frac{\mu}{m\Omega}\Theta_3^1, \tag{II.1.11}$$

$$\left(1 - \frac{1}{\Omega}v_\parallel\Theta_7\right)\dot{\tilde{\theta}} = v_\parallel\Theta_1^2 + \frac{v_\parallel^2}{\Omega}\left(\Theta_2^2 + \Theta_1^2\Theta_7\right) + \frac{\mu}{m\Omega}\Theta_3^2, \tag{II.1.12}$$

$$\left(1 - \frac{1}{\Omega}v_\parallel\Theta_7\right)\dot{\phi} = v_\parallel\Theta_1^3 + \frac{v_\parallel^2}{\Omega}\left(\Theta_2^3 + \Theta_1^3\Theta_7\right) + \frac{\mu}{m\Omega}\Theta_3^3, \tag{II.1.13}$$

$$\left(1-\frac{1}{\Omega}v_{\parallel}\Theta_7\right)\dot{v}_{\parallel}=-\frac{\mu}{m}\Theta_4+\frac{\mu v_{\parallel}}{m\Omega}(\Theta_6-\Theta_4\Theta_7), \tag{II.1.14}$$

where the particle constants of motion are

$$E=\frac{1}{2}mv_{\parallel}^2+\mu\frac{F(s)}{b_3(s,\tilde{\theta})}, \tag{II.1.15}$$

$$P_{\phi}=\frac{f(s)^2}{4\psi_1}+\frac{Bv_{\parallel}b_3(s,\tilde{\theta})}{\Omega}. \tag{II.1.16}$$

The equations which determine the orbits in axis-symmetric time independent magnetic field are integrable and can be obtained from these invariants of motion $(E,\,P_{\phi},\,\mu,\,\sigma)$. The trajectories can be determined analytically along the entire orbit, but the time dependence can only be computed numerically. Eliminating $v_{\parallel}$ from the previous expressions, the orbit can be expressed in terms of the implicit relation

$$\frac{1}{2}m\frac{\Omega^2}{ZeB_{\phi}(s,\theta)^2}\left(P_{\phi}-\psi_1 s^2\right)^2+\mu B(s,\theta)-E=0. \tag{II.1.17}$$

The solution of this equation defines a set of orbits for given $(E,\,P_{\phi},\,\mu)$. When this equation has two different solutions, it is necessary to introduce $\sigma=\mathrm{sign}(\dot{\phi})$ to distinguish them. Each orbit crosses the horizontal mid-plane, defined as the line $(s=1;\theta=\pi)\rightarrow(s=1;\theta=0)$, twice. In order to study the topology of each orbit, the following definitions are introduced allowing for negative s values

$$\tilde{B}(s)=B(s,0)\quad\text{for } s>0;\qquad \tilde{B}(s)=B(s,\pi)\quad\text{for } s<0, \tag{II.1.18}$$

$$\tilde{B}_{\phi}(s)=B_{\phi}(s,0)\quad\text{for } s>0;\qquad \tilde{B}_{\phi}(s)=B_{\phi}(s,\pi)\quad\text{for } s<0, \tag{II.1.19}$$

leading to

$$\tilde{\Phi}(s,E,P_{\phi},\mu)=\frac{1}{2}m\frac{\Omega^2}{Ze\tilde{B}_{\phi}(s)^2}\left(P_{\phi}-\psi_1 s^2\right)^2+\mu\tilde{B}(s)-E=0. \tag{II.1.20}$$

It is assumed that the toroidal field is monotonically decreasing with the major radius and that $B(s,\theta)$ has only one maximum in θ for a given value of s. This allows the analysis of most plasma shapes including elliptic plasmas with high triangularity, but eliminates "bean-shaped" plasmas or strong elliptic plasmas with d-trapped particles [51].

Equation (II.1.7) where $s\in[0,1]$ and $\theta\in[0,2\pi]$, θ being a periodic coordinate, describes the projection of the orbit in the (s,θ) plane; while Eq. (II.1.20) where $s\in[-1,1]$ describes only the crossings of the orbit through the mid-plane of the torus. This equation can have zero to four solutions corresponding to zero to two orbits. The solution of the equation $\tilde{\Phi}(s=\pm1,E,P_{\phi},\mu)=0$ corresponds to orbits of marginally confined particles which cross the plasma boundary, whereas the solution $\tilde{\Phi}(s=0,E,P_{\phi},\mu)=0$ yields the orbits of particles crossing the magnetic axis. The loci of these orbits in $(E,\,P_{\phi},\,\mu)$ coordinates are given by the solution of the two equations

$$\begin{cases}\tilde{\Phi}=0\\ \dfrac{\partial\tilde{\Phi}}{\partial s}=0.\end{cases} \tag{II.1.21}$$

TABLE II.1
Topology Regions of the Particle Orbits

Region	Orbits	Orbit types
I	Two	Co-passing, encircling the axis Counter-passing, encircling the axis
II	Two	Co-passing, encircling the axis Counter-passing, high field side
III	Two	Mirror-trapped, encircling the axis Counter-passing, encircling the axis
IV	Two	Mirror-trapped, encircling the axis Counter-passing, high field side
V	One	Mirror-trapped, encircling the axis
VI	One	Co-passing, encircling the axis
VII	One	Mirror-trapped, not encircling the axis
VIII	One	Co-passing, low field side
IX	No orbits	—

For a given particle energy the different classes of orbits can be traced in the (P_ϕ, μ)-plane. The previous system of equations separates the (P_ϕ, μ)-plane into three regions corresponding to the existence of no orbits, one orbit, or two orbits. The equation $\tilde{\Phi}(s=0, E, P_\phi, \mu)=0$ separates the (P_ϕ, μ)-plane into two different regions related to the topology of the orbit around the axis. By crossing this boundary there is a particle that crosses the magnetic axis and changes from an orbit encircling the axis to an orbit not encircling the axis or vice versa. In order to complete the orbit classification the definition of a mirror-trapped particle is given. The orbit is trapped if $\dot{\phi}$ changes sign during the orbit; if $\dot{\phi}>0$, the particle is co-passing, and if $\dot{\phi}<0$, the particle is counter-passing. The system of equations

$$\begin{cases} \tilde{\Phi}=0 \\ \dot{\phi}(s)=0 \end{cases} \tag{II.1.22}$$

separates the (P_ϕ, μ)-plane into two regions corresponding to the existence of trapped particles. Combining these conditions, nine distinct regions can be considered, as shown in Table II.1. An orbit is considered to encircle the axis if it crosses the mid-plane in $s\in[0, 1]$ and in $s\in[-1, 0]$. An orbit is on the high field side if it crosses the mid-plane twice at $s\in[-1, 0]$ and on the low field side if it crosses the mid-plane twice at $s\in[0, 1]$. The topological transition of the orbits into different regions are described in Table II.2 [43].

The previous analysis considers an unbounded system. However, with the inclusion of a plasma boundary the orbits with increasing values of P_ϕ start leaving the plasma by crossing the plasma boundary.

The solution of the equation $\tilde{\Phi}(s=-1, E, P_\phi, \mu)=0$ creates region b in the (P_ϕ, μ)-plane where an orbit leaves the plasma at the high field of the tokamak. The same happens for the solutions of the equation $\tilde{\Phi}(s=1, E, P_\phi, \mu)=0$; the orbit leaves the plasma at the low field side of the torus thereby creating region c. In region a all possible orbits are inside the plasma boundaries and in region d all orbits leave the plasma or are completely outside. Both these boundaries can subdivide regions I–IX into subregions a, b, c by restricting the number of complete orbits inside the plasma. The exceptions are regions VII and VIII

TABLE II.2
Topological Transitions of the Particle Orbits

Transition	Regions	Orbits
1	I → III	Co-passing, get mirror-trapped
2	III → IV	Counter-passing, crosses the axis
3	I → II	Counter-passing, crosses the axis
4	IV → V	Counter-passing, disappears
5	III → VII	Both orbits turn into a mirror-trapped
6	VII → VIII	Mirror-trapped turn into co-passing
7	VI → VIII	Co-passing, crosses the axis
8	VI → V	Co-passing, get trapped
9	V → VII	Mirror-trapped, crosses the axis
10	II → VI	Counter-passing, disappears
11	VIII → IX	Co-passing, disappears

with orbits only on the low field side which cannot leave the plasma through the high field side. In other words, regions VII.c and VIII.c do not exist according to this classification. Figures II.1–II.2 represent the topology of a particle orbit for a typical JET configuration. In Fig. II.1 a particle with a low energy is considered. For low energy particles the orbits are divided into three groups: co-passing, counter-passing, and trapped orbits. In Fig. II.1 each group of particles is represented as a domain in the magnetic moment and toroidal momentum space. The magnetic moment μ is normalized to the magnetic momentum of a low energy particle located at the magnetic axis with the velocity along the magnetic field equal to zero. The toroidal momentum is normalized to the toroidal momentum of a low energy particle following the flux surface that determines the plasma boundary. In Fig. II.2

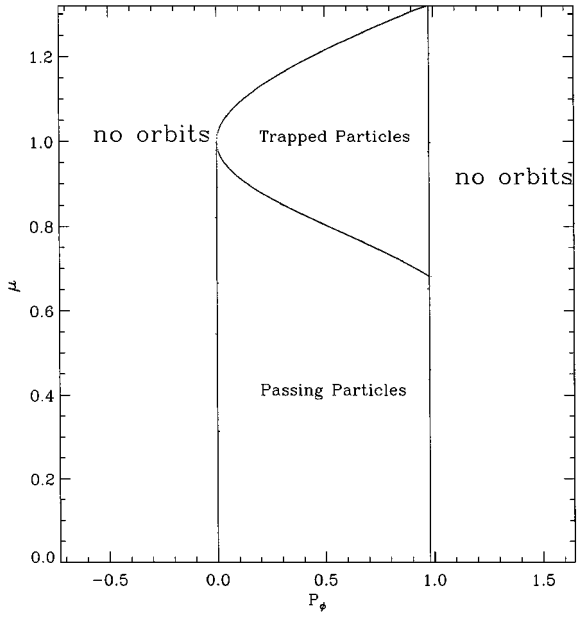

FIG. II.1. The topology of standard orbits for a given particle energy as a function of the magnetic moment and toroidal canonical momentum.

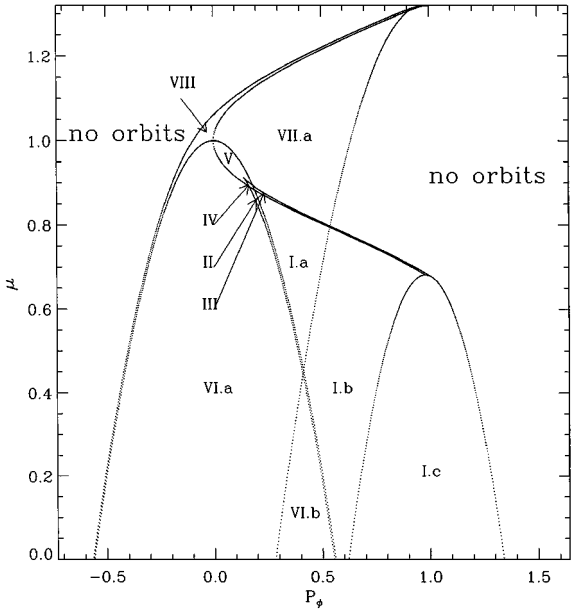

FIG. II.2. The topology of non-standard orbits for a given particle energy as a function of the magnetic moment and toroidal canonical momentum.

the topology of the orbits of an alpha particle with 3.5 MeV of energy is represented for different values of the magnetic moment and the toroidal momentum with the same normalization used in Fig. II.2. The class of orbits corresponding to each subregion in (P_ϕ, μ) space is shown in Table II.1.

III. NUMERICAL PROCEDURE

III.1. *Code Organization*

Equilibria are constructed using the code HELENA [26], which solves the Grad–Shafranov equation in the (R,Z)-plane by means of isoparametric bicubic Hermite finite elements. The linear properties of the toroidal Alfvén eigenmode spectrum are determined by the normal-mode code CASTOR (*c*omplex *A*lfvén *s*pectrum in *toro*idal geometry) [31]. In addition, the ideal MHD continuous spectrum in advance at each flux surface is solved independently by the code CSCAS [40].

The MHD eigenmodes obtained can experience fluid damping due to conversion of the mode energy into strongly damped kinetic Alfvén waves (radiative damping) [35] and collisional electron damping [44].

The resonant energy exchange between the linear eigenmode and the different particle species present in the plasma, including bulk ions and energetic particles, can only be computed by a gyro-kinetic approach. The gyro-kinetic extension of the CASTOR code (CASTOR-K code, Diagram III.1a) evaluates numerically the quadratic form δW_{hot}, which represents the contribution of resonant particles to the stability of the Alfvén eigenmodes. It includes the determination of the principal wave damping mechanisms: ion and electron Landau damping, radiative damping, and collisional electron damping as well as the evaluation of the instability drive (Diagram III.1b).

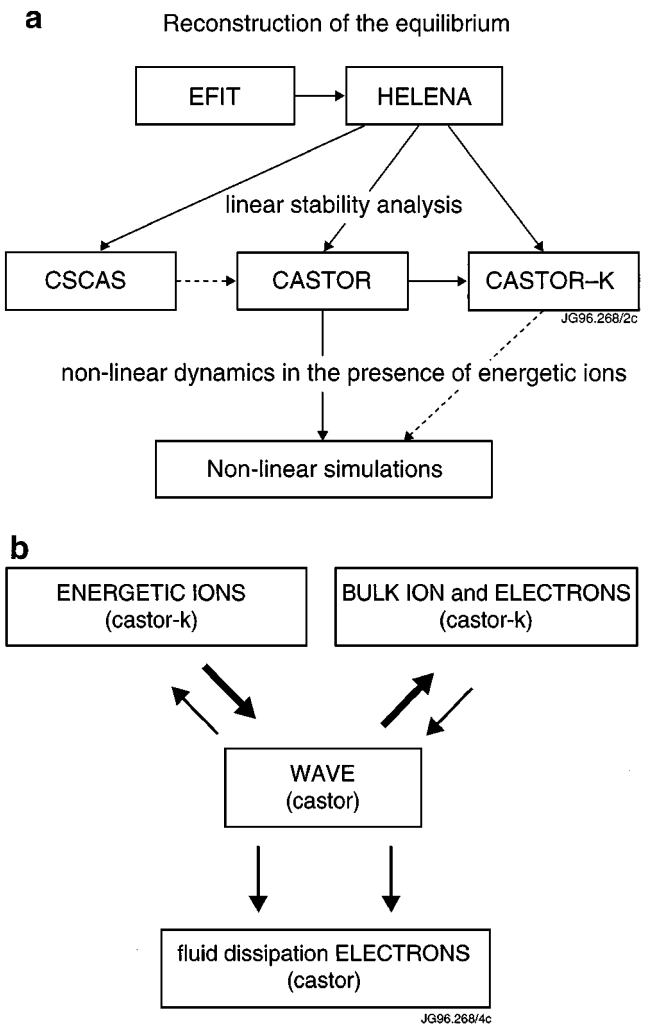

DIAGRAM III.1. (a) The different levels of the gyro-kinetic model together with the corresponding numerical tools. (b) The wave exchanges energy with the different particle species present in the plasma. The mode becomes unstable when the energy gained by the wave from the energetic particles exceeds the energy lost to bulk ions and electrons.

III.2. *Ideal and Nonideal MHD*

The kinetic Alfvén wave spectrum is computed by the nonideal extension of the CASTOR code. A small change in the induction equation allows the kinetic effects to be modelled with accuracy. Using the fact that CASTOR is a resistive MHD code the kinetic terms can be simply introduced by generalizing the dissipation into a complex parameter. By modeling the kinetic corrections using a simple complex parameter, a correct result is obtained in the gap where $k_{\|} \approx 1/2qR_0$. q is the safety factor and R_0 is the major radius. This approximation is sufficient to compute the KTAE spectrum in full toroidal geometry since the kinetic corrections are valid in the gap region where they are important. Furthermore, the coupling between TAEs and kinetic Alfvén waves leads to conversion of energy from TAEs into kinetic Alfvén waves inside the gap region. Although the propagation of the kinetic Alfvén wave across the entire plasma cross-section is not accurately described, the energy

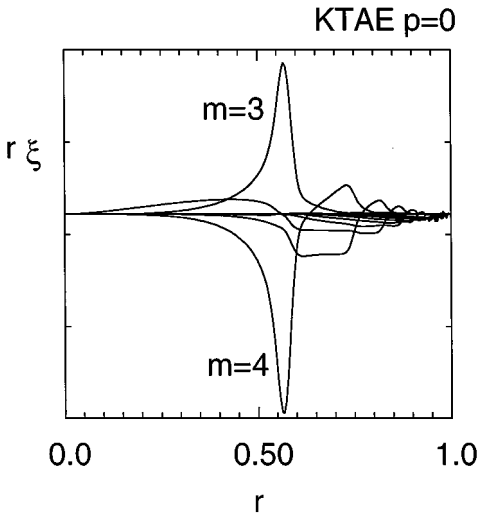

FIG. III.2.1. The radial displacement of a KTAE computed by the CASTOR code. The eigenfunction represents a mode with radial mode number $p = 0$.

transferred from the TAE to the KAW is accurate. Since these kinetic waves are strongly damped, the radiative damping can also be described well within this approximation.

First order FLR effects of core ions and $E_\parallel \neq 0$ give the corrections to the eigenmode equation in the boundary layer around the TAE resonance region.

The structure of this equation is analogous to the structure of the resistive MHD equations in the limit of $|c^2\eta k_r^2/4\pi\omega| \ll 1$ with a general complex parameter $\tilde{\eta}$ defined by

$$\tilde{\eta} = 4\pi\omega\rho_s^2\delta(v_e) + i4\pi\omega\left(\frac{3}{4} + \frac{T_e}{T_i}\right)\rho_s^2. \qquad \text{(II.1.23)}$$

Thus, CASTOR provides the MHD spectrum including the TAE and KTAE field perturbations needed in CASTOR-K. Using this approximation the KTAE spectrum in full toroidal geometry is computed.

The structure of the KTAE modes, where full toroidal effects are taken into account, is shown in Figs. III.2.1–III.2.4. The calculations are performed for a JET-shaped equilibrium with $R_0 = 3m$, the safety factor varying from $q_0 \approx 1$ to $q_{\text{edge}} \approx 3$ and the normalized complex parameter $\tilde{\eta}/(\mu_0 R_0 v_A) = 10^{-7} + 10^{-6}i$. v_A denotes the Alfvén velocity on the magnetic axis. The inner structure of these modes is similar to the structure of the modes computed using the simplified analytic models, but the global structure of the full toroidal modes is more complex as can be seen in Figs. III.2.1–III.2.4.

III.3. *The CASTOR-K Code*

The influence of energetic particles on the stability of Alfvén waves is evaluated. Instabilities exist if the energy transferred from energetic particles into the mode via inverse Landau damping exceeds the energy dissipated into the bulk ions and electrons. The CASTOR-K code computes perturbatively the energy exchange between a given MHD eigenfunction and a distribution of energetic particles (see Diagram III.3). The energy transferred can be expressed by the inner product between the perturbed Lagrangian and the perturbed distribution function. This implies a six-dimensional integration over the phase-space based on

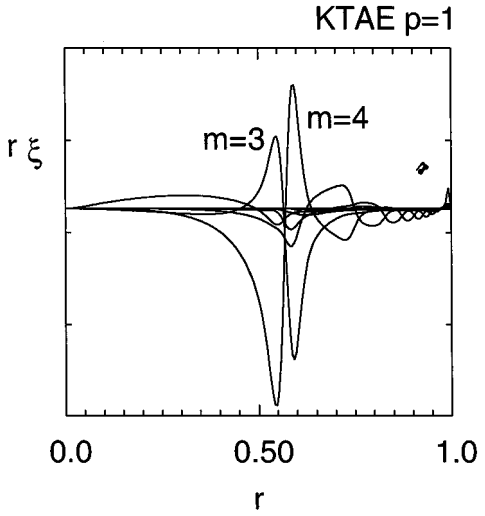

FIG. III.2.2. The radial displacement of a KTAE computed by the CASTOR code. The eigenfunction represents a mode with radial mode number $p = 1$.

the coordinates E, P_ϕ, μ, τ, α, and ϕ, which is related to the usual coordinates $(\vec{x}, \vec{v})$ by the Jacobian

$$d^3x\, d^3v = \frac{1}{m^2 Ze} dE\, dP_\phi\, d\mu\, d\tau\, d\alpha\, d\phi. \tag{III.3.1}$$

The phase-space integration is performed using both numerical and analytical procedures. The gyro-averaged description of the motion of the guiding center averages the gyro-angle contribution in the integration

$$\int L^{(1)} d\alpha = 2\pi L^{(1)}. \tag{III.3.2}$$

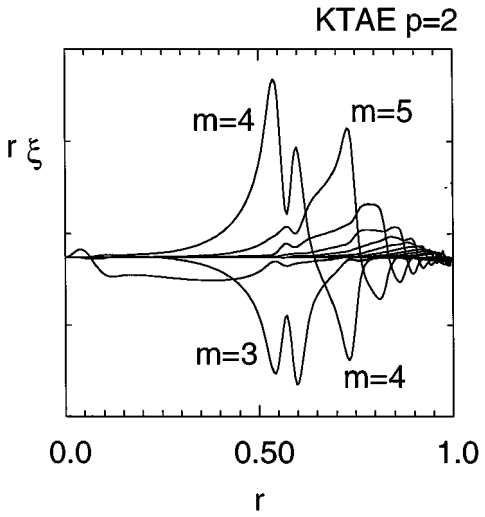

FIG. III.2.3. The radial displacement of a KTAE computed by the CASTOR code. The eigenfunction represents a mode with radial mode number $p = 2$.

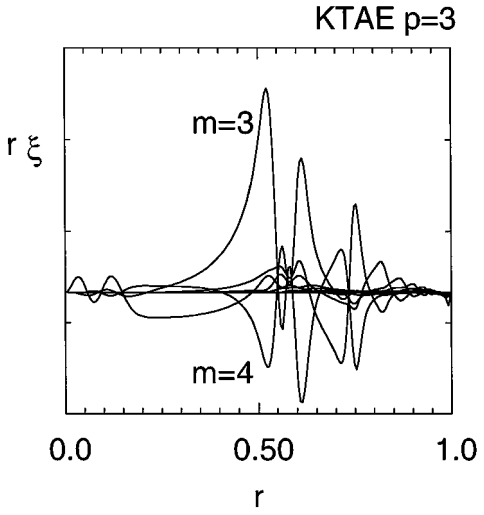

FIG. III.2.4. The radial displacement of a KTAE computed by the CASTOR code. The eigenfunction represents a mode with radial mode number $p = 3$.

Exploiting the periodicity of the unperturbed orbits in the poloidal coordinate, the perturbed Lagrangian is decomposed in Fourier harmonics Y_p and the poloidal angle integration is performed using Fourier transforms. Only periodic perturbations in the toroidal direction are considered, thus the integration over the toroidal angle is performed analytically

$$\int e^{-in\phi} L^{(1)} e^{in\phi} d\phi = 2\pi L^{(1)}. \tag{III.3.3}$$

In the analysis of the energy exchange between the particle and the wave only the resonant part of the integral is required. The energy integration is performed analytically over the pole contributions,

$$\mathrm{Im}\left[\int \frac{d\tilde{E}\, d\tilde{P}_\phi\, d\tilde{\mu}}{\Gamma(\tilde{E})}\right] = \int d\tilde{P}_\phi\, d\tilde{\mu} \frac{2\pi}{|\partial\Gamma/\partial\tilde{E}|_{(\Gamma(\tilde{E})=0)}}. \tag{III.3.4}$$

The remaining two integrations over (P_ϕ, μ) are performed numerically using a specific algorithm developed for this problem. The scheme applied to the phase-space integration is summarized in Table III.3.1.

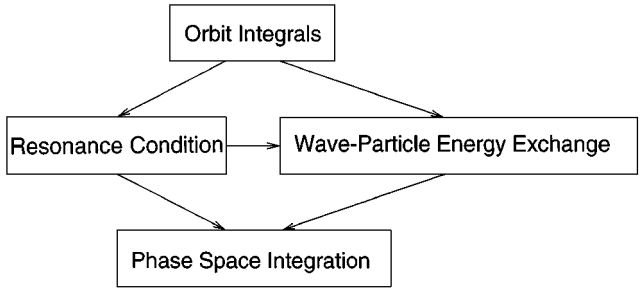

DIAGRAM III.3. The three main stages of the calculation performed by the CASTOR-K code.

TABLE III.3.1
Scheme Applied to the Phase-Space Integration

The gyro-angle	α	Analytical	Average procedure
The poloidal angle	θ	Numerical	Fourier transform
The toroidal angle	ϕ	Analytical	Fourier decomposition
The energy	E	Analytical	Integration over the poles
The magnetic moment	μ	Numerical	Binary search algorithm
The toroidal canonical momentum	P_ϕ	Numerical	Binary search algorithm

The two-dimensional integration must be performed for several values of $\tilde{p}$ and σ,

$$\int d\tilde{P}_\phi \, d\tilde{\mu} \tilde{\tau}_b (\omega - n\omega_*) \frac{\partial F}{\partial \tilde{E}} \frac{|Y_{\tilde{p}}|^2}{|\partial \Gamma / \partial \tilde{E}|}. \tag{III.3.5}$$

The computation of the integrand involves considerable numerical effort. The $Y_{\tilde{p}}$ coefficients require the integration of the resonant unperturbed orbits and the Fourier transforms of the perturbed Lagrangian. The selection of the resonant orbits is computed numerically using a root finding procedure; the contribution from each pole is evaluated numerically in the form of $\partial\Gamma/\partial\tilde{E}$. Since the computational effort of each contribution to the total (P_ϕ, μ) integration is significant, the numerical procedure should make a good selection of the points in which the integrand is evaluated.

III.4. *Integration of the Particle Orbits*

The trajectory of a particle can be expressed analytically as a function of the invariants of motion and of the equilibrium quantities. The time dependence of the particle trajectory must be integrated numerically. For this purpose an explicit integration procedure is developed. The accuracy of the integration scheme is such that the orbit trajectory is reproduced up to a given tolerance. The procedure automatically adjusts the time step according to the conservation of the invariants, namely the energy E and the toroidal canonical momentum P_ϕ. The conservation of the magnetic moment is always guaranteed by the gyro-averaged equations of motion. A fourth-order Runge–Kutta algorithm [1] is suitable for this problem with a good compromise between accuracy and efficiency. Using this procedure an accuracy of $\epsilon_E \approx 10^{-10}$ can be achieved with less than 100 time steps per orbit for most orbits. In order to obtain the orbit trajectory up to machine precision $\epsilon_E \approx 10^{-15}$ (double precision), around 1000 time steps per orbit are required. Unfortunately, this is not true for all orbits. The orbits very close to the bifurcation where a trapped orbit becomes a passing orbit are called pinch orbits. These orbits are very difficult to compute numerically. For this class of orbits the bounce time diverges and those orbits cannot be computed accurately. Since in most applications the contribution of particles at the trapped-passing boundary is not important, these particles are neglected in the calculations. Another class of particles that can create problems during the integrations are the particles that cross the magnetic axis. Polar coordinates are very efficient in calculating most of the trajectories, but in the plasma center $s = 0$ the equation of motion becomes singular, i.e., $\dot{\theta} \to \infty$. The sharp transition from $\theta = \pi$ to $\theta = -\pi$ of the polar coordinate when the orbit crosses the axis requires a very small time step to resolve it. The automatic step adjusting procedure can solve the problem but requires an increasing number of time steps as the particles get closer and

closer to the magnetic axis, thereby making this procedure very inefficient. The solution is to adopt a double coordinate integration procedure using both poloidal and Cartesian coordinates. By solving 6 equations instead of the usual 4,

$$\begin{cases} \dot{s} = F_s(s, \theta, v_\parallel) \\ \dot{\theta} = F_\theta(s, \theta, v_\parallel) \\ \dot{\phi} = F_\phi(s, \theta, v_\parallel) \\ \dot{v}_\parallel = F_v(s, \theta, v_\parallel) \\ \dot{X} = \dot{s}\cos\theta - s\dot{\theta}\sin\theta \\ \dot{Y} = \dot{s}\sin\theta + s\dot{\theta}\cos\theta \end{cases} \tag{III.4.1}$$

the coordinate system is changed into a Cartesian coordinate system when a particle gets close to the magnetic axis. Therefore, without any significant increase in the computational overhead the orbits close to the magnetic axis can be computed accurately. The overall accuracy can be seen in Fig. III.4.1 where the error associated with the conservation of the invariants is displayed as a function of the number of time steps per orbit used in the calculation and for different numbers of orbits computed. The larger the number of orbits is, the larger the associated error becomes. By introducing a fourth-order method the error decreases with the fourth power of the time step. This should be true for half an orbit. If an entire orbit is computed the error scales as $\epsilon \propto (\Delta t)^{-4.33}$ due to the up–down symmetry of the orbit as shown in Table III.4.1. For a larger number of orbits the error scaling is also given by Table III.4.1.

For an asymptotically large number of orbits the error should scale as $\epsilon \propto (\Delta t)^{-5}$ due to the periodicity of the orbits. Using up–down symmetric plasmas only half of the orbits need to be computed.

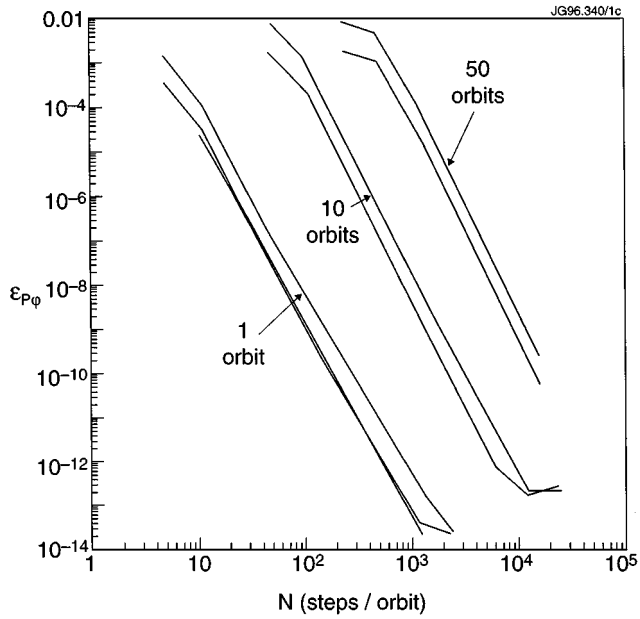

FIG. III.4.1. Error associated with the conservation of the invariants (E, P_ϕ) as a function of the number of time steps per orbit.

TABLE III.4.1
Error in the Orbit Integrations

Number orbits	Integration error
1	$\epsilon \propto (\Delta t)^{-4.33}$
10	$\epsilon \propto (\Delta t)^{-4.77}$
50	$\epsilon \propto (\Delta t)^{-4.94}$

III.5. *Numerical Integration of δW_{hot} in the Subspace P_ϕ, μ*

The integration over the (P_ϕ, μ) coordinates is performed using a two-dimensional adaptive scheme. The procedure works in two phases. At first a rectangular mesh is constructed evaluating the function to be integrated at each point. Thus, a first estimate of the integral is obtained. In the second step, a refinement criterion selects the area where accumulation points are required for improvement in the accuracy of the integration. This procedure is repeated until a predefined accuracy of the integration is achieved. This method is useful in cases where the integral evaluations are very demanding in terms of computing time and where it pays off to spend some time selecting the points at which the integrand is to be evaluated. The mesh accumulation is concentrated in areas where the function is less well behaved and, hence, the contribution to the overall integration is more important. The method is a two-dimensional equivalent of the Simpson rule [1], where the evaluated points are fitted using cubic polynomials. The deviation from the bicubic interpolating function is a measure of the error associated with the integration of that particular sub-element. This deviation function is used to decide which divisions require further subdivisions to achieve a given accuracy in the integration. Each division requires nine evaluations of the integrand and each subdivision requires an additional five evaluations of the integrand. The number of subdivisions required depends on the behavior of the integrand and the success of the method depends on the choice of the initial rectangular mesh. This method has the advantage of giving the result after each subdivision and of providing an estimate at each step of the calculation. Convergence studies show an error estimate scaling consistent with a second order method in two dimensions

$$\epsilon = (\text{points})^{-1}. \tag{III.5.1}$$

In Figs. III.5.1–III.5.3 the steps of the numerical integration procedure are presented. The results of the test case are shown in Fig. III.6.1 where the corresponding value of $\frac{v_\alpha}{v_A} = 1$ is used with the parameters of Table III.6.1. The initial rectangular mesh is represented in Fig. III.5.1. This regular mesh enables a crude estimate of the final result but, also, forms a basis for the algorithm which calculates the optimum mesh accumulation, as shown in Fig. III.5.4. After several iterations, as shown in Fig. III.5.2, the mesh is accumulated in an area corresponding to the largest values assumed by the integrand as seen in Fig. III.5.5. A further refinement of the mesh is shown in Fig. III.5.3 and the final result is displayed in Fig. III.5.6. This simple test case illustrates the numerical procedure, but typical tokamak applications involve more complex functions which require a finer mesh and a more elaborate initial mesh to guarantee that all the details of the integrand can be resolved.

In Fig. III.5.7 the error associated with the numerical integration as a function of the number of steps is represented. Logarithmic scales are used, and a linear fit is displayed

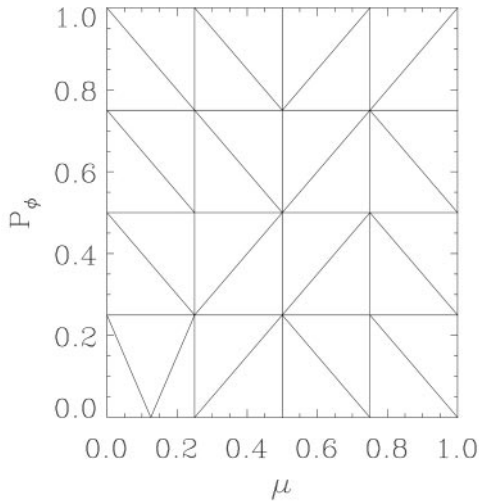

FIG. III.5.1. Map of the integration grid with 25 points without any mesh accumulation.

in order to represent the asymptotic behavior. In Fig. III.5.8 the error associated with the numerical integration as a function of the number of points is represented. One of the key issues while implementing such a method is to guarantee that the same point is not evaluated twice, since each evaluation is costly in terms of computing time. This problem is solved by storing the integrand in a vector and using it whenever required. In order to optimize the storage as well as the retrieval of the information, a reversed binary index of all the rational points in a square is introduced. Hence, the point $\{0.0, 0.0\}$ is represented by the pair $(1, 1)$, $\{0.0, 1.0\} \rightarrow (1, 0)$, $\{1.0, 0.0\} \rightarrow (0, 1)$ and $\{1.0, 1.0\} \rightarrow (0, 0)$. Successive subdivision of the interval yields the coordinates for $\{0.5, 0.0\} \rightarrow (2, 0)$, $\{0.25, 0.0\} \rightarrow (3, 0)$, $\{0.75, 0.0\} \rightarrow (7, 0)$, etc. This enables a binary search for the information as demonstrated in Fig. III.5.9.

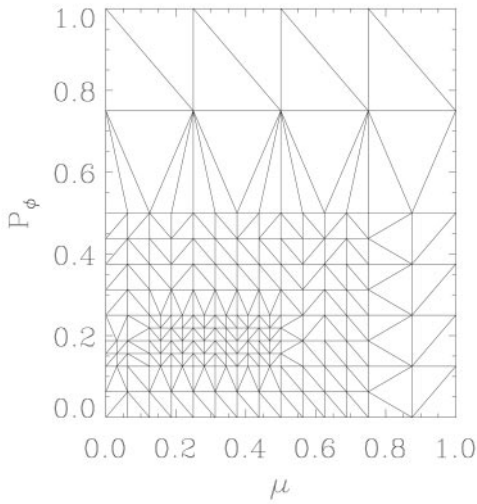

FIG. III.5.2. Map of the integration grid with 185 points and with mesh accumulation.

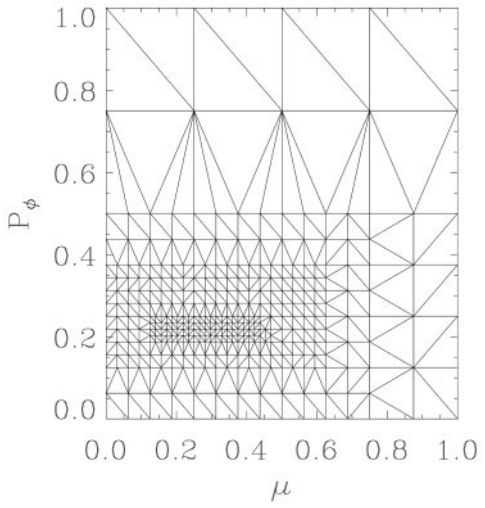

FIG. III.5.3. Map of the integration grid with 345 points and with mesh accumulation.

III.6. *Benchmark Tests*

The accuracy of the CASTOR-K code is assessed by comparison with analytic theory in the small orbit width limit and by a benchmark test with linear [20] and non-linear simulations [5]. For comparison with the local analytic expression, valid in the small orbit and large aspect ratio limit, a very large aspect ratio is chosen. In order to ensure that

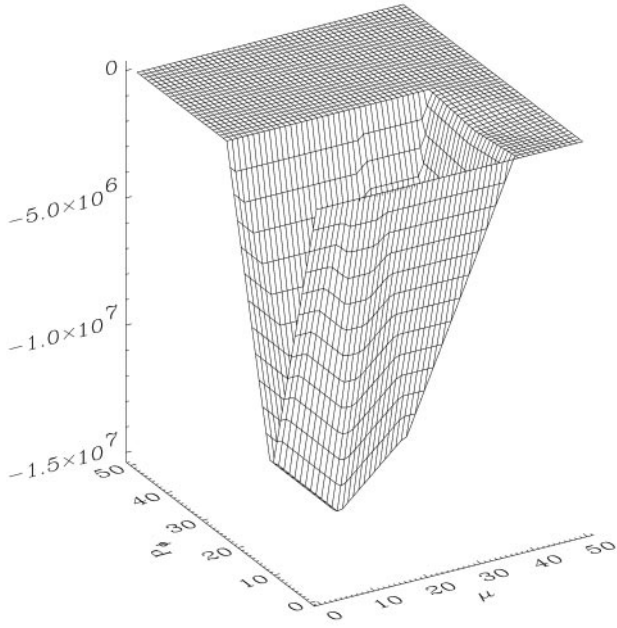

FIG. III.5.4. Surface plot of the integrand evaluated at the 25 grid points without any mesh accumulation as shown in Fig. III.5.1.

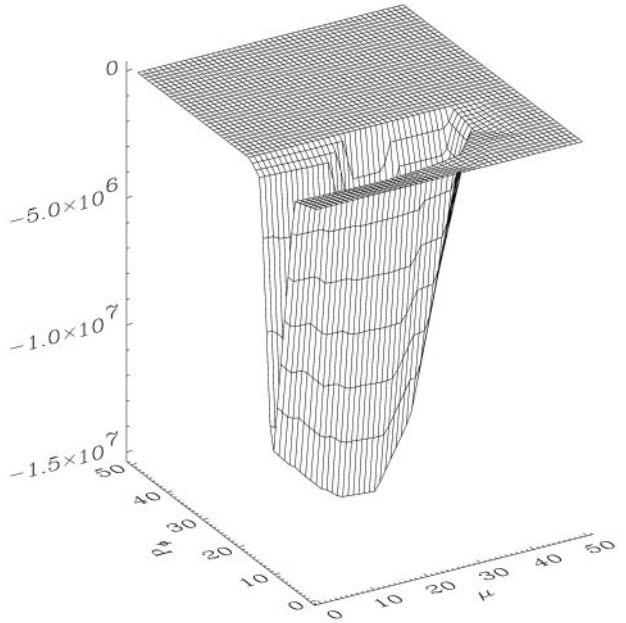

FIG. III.5.5. Surface plot of the integrand evaluated at 65 grid points using mesh accumulation.

the small orbit limit can be applied an extremely large value for the magnetic field is chosen. In addition, a very localized eigenfunction is used in the calculation where the radial displacement is set to zero $\xi_r = 0$ in agreement with the condition $\xi_r \ll \xi_\theta$. An overview of these parameters is given in Table III.6.1.

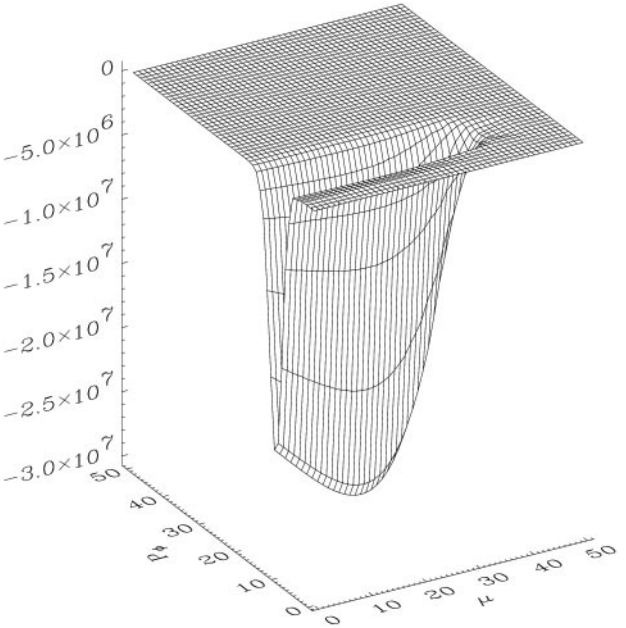

FIG. III.5.6. Surface plot of the integrand evaluated at 425 grid points using mesh accumulation.

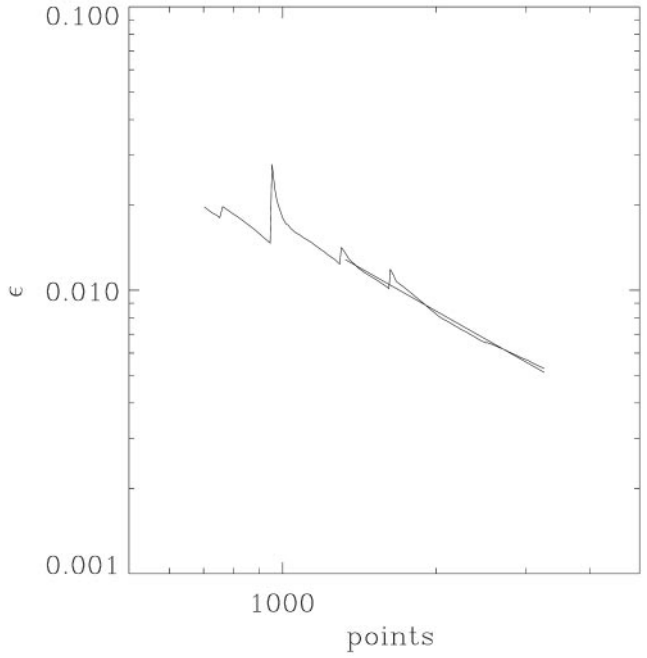

FIG. III.5.7. Error associated with the two-dimensional integration as a function of the number of evaluations represented in a logarithmic scale.

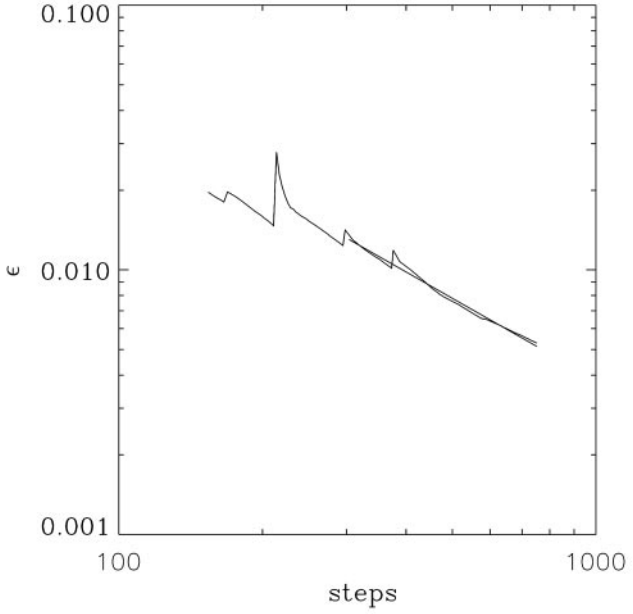

FIG. III.5.8. Error associated with the two-dimensional integration as a function of the number of iterations represented in a logarithmic scale.

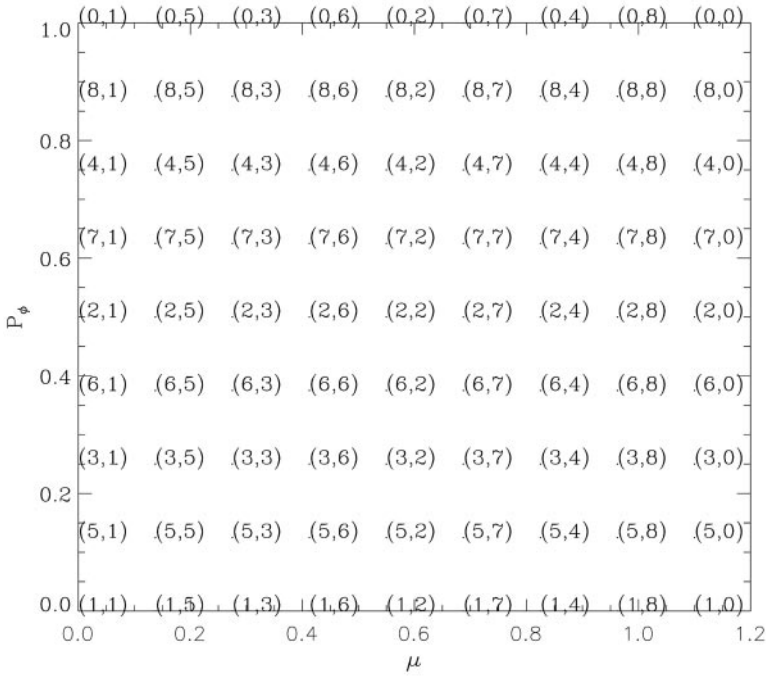

FIG. III.5.9. Map of the initial distribution of the integrand evaluations and their binary coordinates.

Using these parameters the known results obtained in the small orbit limit and large aspect ratio limit are recovered. Figure III.6.1 compares the results obtained from analytic theory [3] with those calculated by the CASTOR-K code. This diagram shows a good numerical convergence, where an accuracy of 1% can be achieved with around 1000 evaluations of the integrand. This calculation will take around 10–20 minutes on a desktop personal computer based on a Intel pentium microprocessor running at 400 MHz (SPECint95 of 15.0 and CPUmark32 of 1000), under the Linux operating system. Realistic tokamak simulations can take up to a few hours of CPU time depending on the complexity of the orbits, the eigenfunctions, and on the accuracy required.

In the comparison with the initial value simulations non-linear code (FAC) a very unstable mode is considered. This allows a sufficiently accurate determination of the growth rate with a simulation of a few wave periods in the non-linear initial value calculation. It is important that the growth rate be sufficiently smaller than both the particle bounce frequency and the

TABLE III.6.1
Parameters for the Comparison with Analytic Theory

Inverse aspect ratio of the torus	$\frac{1}{\epsilon} = 1 \times 10^3$
Magnetic field on axis	$B_0 = 1 \times 10^9$ T
Major radius of the torus	$R_0 = 8$ m
Bulk ion density	$n_I = 1.3593 \times 10^{36}$ m^{-3}
Total poloidal magnetic flux	$\hat{\psi}_p = .4276 \times 10^{-6}$
Total poloidal magnetic flux	$\psi_p = 2.7367 \times 10^4$ Tm^2
Mode angular frequency	$\omega = 7.08 \times 10^5$ rads^{-1}
Toroidal mode number	$n = -3$
Fast ion temperature (MAXWELLIAN)	$T_\alpha = 1.7500 \times 10^3$ keV

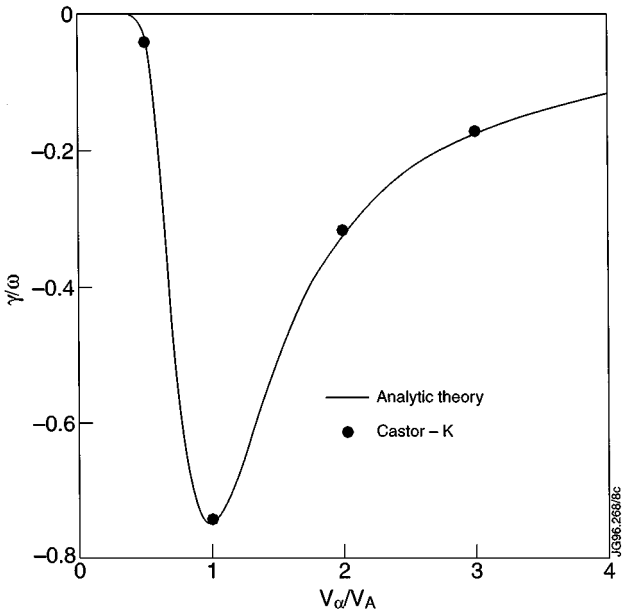

FIG. III.6.1. Comparison of the CASTOR-K code with the results obtained from analytic theory in the small inverse aspect ratio limit.

wave frequency. This is achieved with a high-n TAE. The poloidal mode structure is also simplified by retaining only the dominant poloidal mode components $\tilde{m} = 8, 9$. In tokamak simulations, all relevant poloidal components are included as shown in Figs. III.2.3–III.2.4.

In Fig. III.6.2 the comparison of the CASTOR-K code with the non-linear simulations performed by the FAC code is displayed [5]. The corresponding parameters are listed in

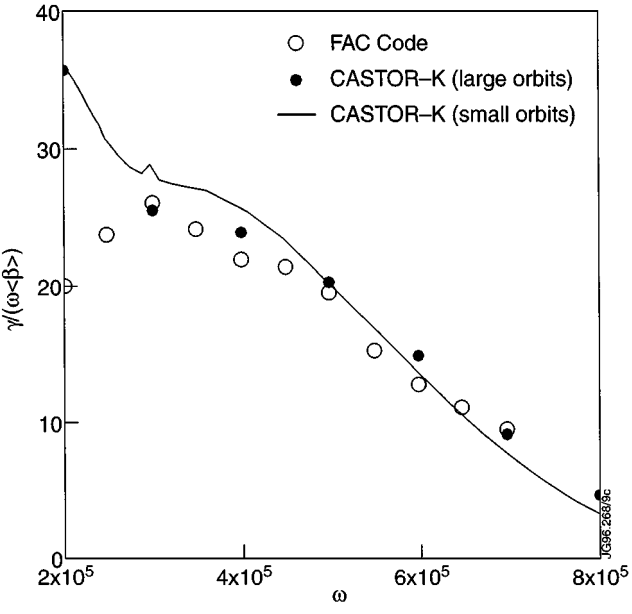

FIG. III.6.2. Comparison of the CASTOR-K code with the non-linear code FAC.

TABLE III.6.2
Parameters for the Comparison with the Non-linear Simulations

Aspect ratio of the torus	$\epsilon = 0.375$
Magnetic field on axis	$B_0 = 6$ T
Major radius of the torus	$R_0 = 8$ m
Bulk ion density	$n_I = 1.0 \times 10^{20}$ m^{-3}
Mode angular frequency	$\omega = 7.000 \times 10^5$ rads^{-1}
Toroidal mode number	$n = -10$
Poloidal mode number	$\tilde{m} = 8, 9$

the Table III.6.2. In this figure the results obtained within the small orbits version of the CASTOR-K code and in the large orbits version of the CASTOR-K code are plotted together with the results obtained by the FAC code. The agreement is excellent within a few percent except for small frequencies where the different specifications of the distribution functions in the CASTOR-K and FAC is important. The small difference between the results from the small orbit's code and the large orbit's code is due to the fact that the orbit's size is small compared with the mode width for the parameters used in this simulation.

In addition, a comparison between the CASTOR-K code and the NOVA-K code [20, 52] developed at the Princeton Plasma Physics Laboratory is performed in the small orbit limit. The main parameters used in the comparison are shown in Table III.6.3, and the results in Fig. III.6.3. It is evident that the agreement with different numerical methods is good.

III.7. *The Influence of Trapped and Passing Particles*

In the small orbit width limit the interaction of a TAE with both passing and trapped particles is calculated for an equilibrium with circular cross-section and inverse aspect ratio $\epsilon = \frac{1}{3}$. A Maxwellian distribution function is used where the thermal velocity coincides with the Alfvén velocity. The TAE component $n = -3$, $\tilde{m} = 3$ is in resonance with co-passing particles with $v_\parallel = -V_A$; and the $n = -3$, $\tilde{m} = 4$ component is in resonance with counter-passing particles with $v_\parallel = V_A$. For the chosen thermal particle velocity these two contributions are the most important ones, accounting for more than 70% of the total energy exchange. The TAE also interacts with trapped particles via the first and second harmonic of the bounce resonance. In Figs. III.7a–III.7d the different classes of particles are represented,

TABLE III.6.3
Parameters for the Comparison with the NOVA-K Model

Aspect ratio of the torus	$\epsilon = 0.300$
Magnetic field on axis	$B_0 = 3$ T
Major radius of the torus	$R_0 = 3$ m
Bulk ion density	$n_I = 5 \times 10^{19}$ m^{-3}
Mode angular frequency	$\omega = 6.000 \times 10^5$ rads^{-1}
Toroidal mode number	$n = -2$
Poloidal mode number	$\tilde{m} = 3, 4$

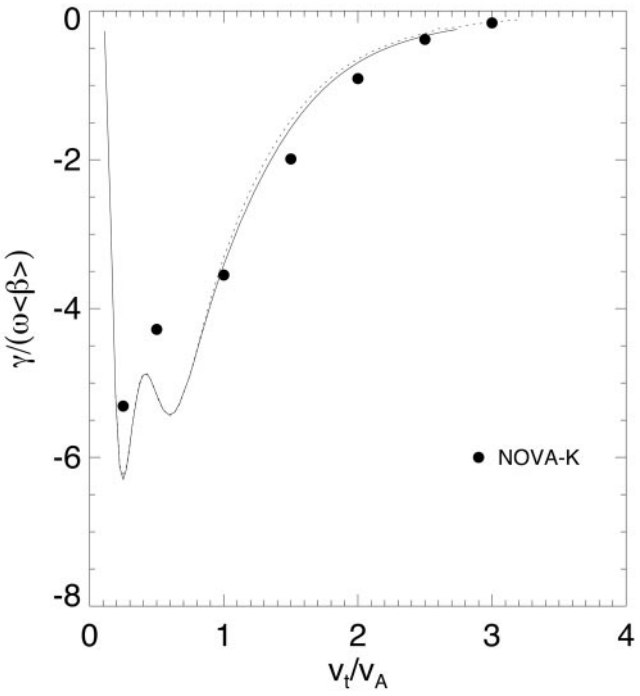

FIG. III.6.3. Comparison of the CASTOR-K with the NOVA-K code.

which interact with the TAE. The contours show the areas in the phase-space where the energy exchange is more pronounced as a function of the toroidal momentum and magnetic moment. The contribution of each resonance to the energy exchange between the particles and the TAE is summarized in Table III.7.1.

In each calculation it is crucial to ensure that a sufficient number of bounce harmonics are kept to guarantee convergence. The number of bounce harmonics required depends on the mode structure and on the nature of the orbits. In this case the nine bounce harmonics shown in Table III.7.1 are sufficient since the contribution of the bounce harmonics with $p > 5$ and $p < -4$ can be neglected. In the case of large orbits and large toroidal mode numbers, the numbers of bounce harmonics have to be increased considerably.

TABLE III.7.1
Contribution of Different Classes of Particles to the Energy Exchange

$p = -3$	34.5%	Passing particles	$v_\parallel = V_A$
$p = -2$	3.2%	Passing particles	$v_\parallel = -\frac{V_A}{3}$
$p = -1$	≈0%	—	—
$p = 0$	≈0%	Trapped particles	Precession drift resonance
$p = 1$	8.1%	Trapped particles	First bounce resonance
$p = 2$	7.6%	Trapped particles	Second bounce resonance
$p = 3$	1.6%	Trapped particles	Third bounce resonance
$p = 4$	42.7%	Passing particles	$v_\parallel = -V_A$
$p = 5$	1.6%	Passing particles	$v_\parallel = \frac{V_A}{3}$

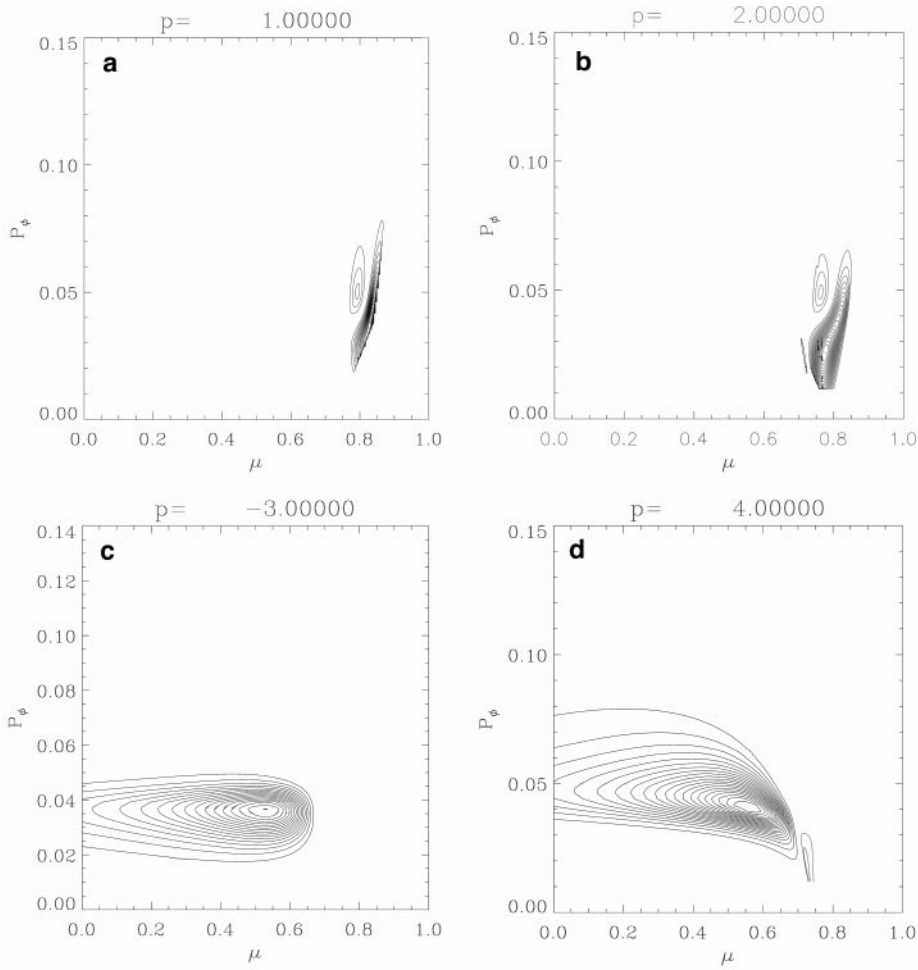

FIG. III.7. (a) Interaction of a TAE with $n = 3$, $\tilde{m} = 3, 4$, with an ion Maxwellian distribution via the first trapped bounce resonance. (b) Interaction of a TAE with $n = 3$, $\tilde{m} = 3, 4$, with an ion Maxwellian distribution via the second trapped bounce resonance. (c) Interaction of a TAE with $n = 3$, $\tilde{m} = 3, 4$, with an ion Maxwellian distribution via the co-passing $v_\parallel = V_A$ bounce resonance. (d) Interaction of a TAE with $n = 3$, $\tilde{m} = 3, 4$, with an ion Maxwellian distribution via the counter-passing $v_\parallel = -V_A$ bounce resonance.

III.8. *The Influence of Large Orbits*

In the case of large orbits, the particles drift away from the flux surfaces and the interaction with a localized mode is significantly reduced. In Figs. III.8a–III.8f the poloidal cross-section of the energy density of a field perturbation is displayed interacting with a Maxwellian distribution of particles for different values of the Larmor radius. The figures also represent the orbit of the particle that exchanges the most energy with the wave. For small values of the Larmor radius, Figs. III.8a–III.8b, the orbits are confined to a flux surface and they exchange energy with the mode very effectively. With increasing Larmor radius, Figs. III.8c–III.8e, the orbits experience excursions away from the flux surfaces decreasing the interaction with the mode. In this regime the precession drift frequency is comparable with the transit and bounce frequencies.

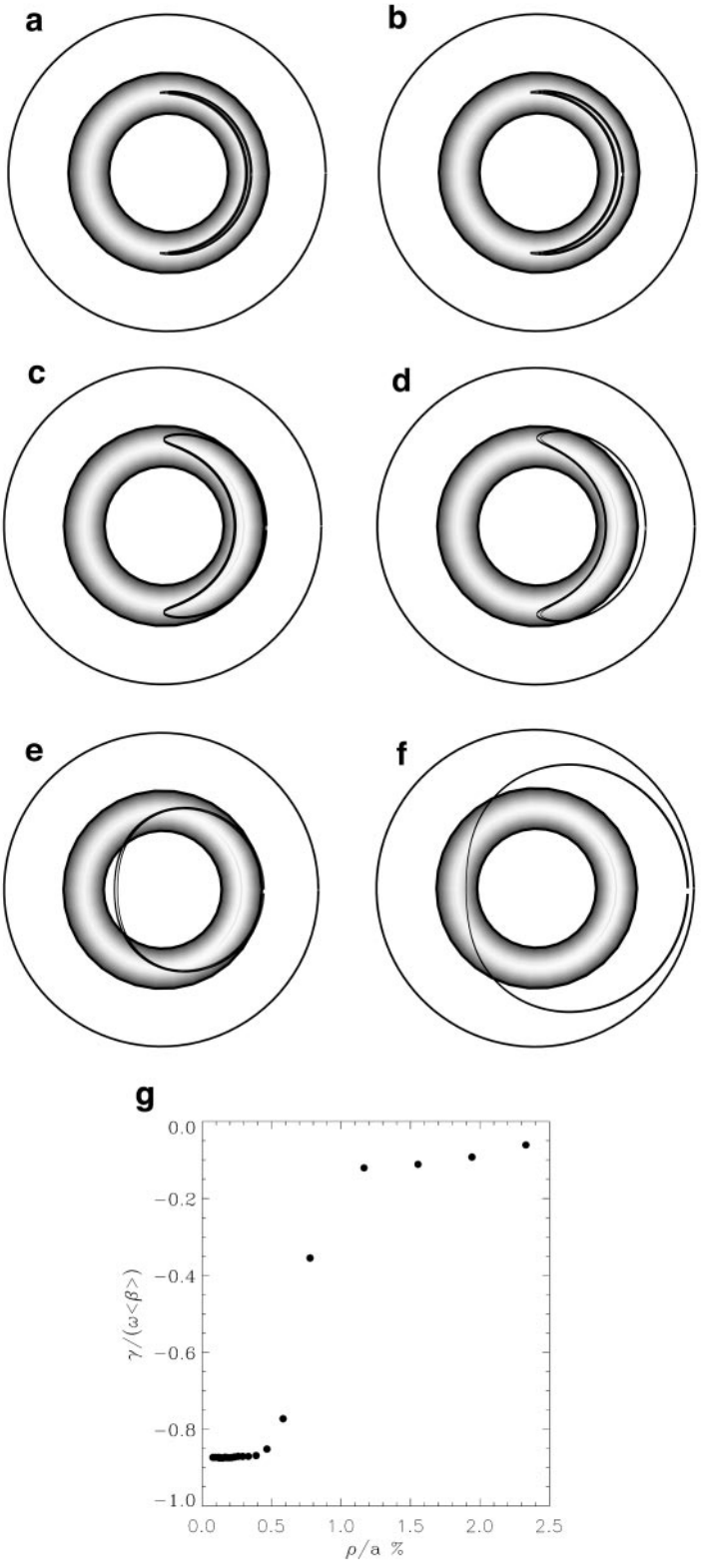

FIG. III.8. (a) $\frac{\rho}{a} = 0.1\%$. (b) $\frac{\rho}{a} = 0.2\%$. (c) $\frac{\rho}{a} = 1.1\%$. (d) $\frac{\rho}{a} = 1.5\%$. (e) $\frac{\rho}{a} = 2.3\%$. (f) $\frac{\rho}{a} = 4.6\%$. (g) Interaction of a MHD wave harmonic $n = 3$, $\tilde{m} = 3, 4$, with particle distributions having different orbit widths represented by ρ_{th}/a.

Finite orbit effects start to reduce the energy exchange between the wave and the particle significantly when the mode width is comparable with the orbit banana width as shown in Fig. III.8d. By further increasing the Larmor radius the trapped banana orbits become non-standard potato orbits as shown in Fig. III.8e. In this case the orbits only cross the perturbation during a short period of time and the energy exchange is very small. This effect is more important for high energy particles close to the magnetic axis. The orbits can be made larger by decreasing the field or the plasma current. The energy exchange between the wave and the particle distribution with different Larmor radii is summarized in Fig. III.8g. The energy exchange between the particles and the wave decreases with increasing normalized Larmor radius of the energetic particles [49]. In Fig. III.8g the energy exchange is represented by the damping of the wave in the presence of an isotropic distribution of particles without spatial gradients.

IV. CONCLUSIONS

The hybrid gyro-kinetic MHD model described in this paper provides a detailed description of the interaction of energetic ions with global plasma waves including realistic geometry together with the finite orbit widths effects for large non-standard orbits. A general self-consistent formulation is derived and the appropriate numerical algorithms for the large scale numerical evaluation are developed and tested. The perturbative approach is used to study the influence of energetic ions on the stability of Alfvén eigenmodes. The ideal MHD model is extended in order to include the effect of a perturbed parallel electric field and of the finite Larmor radius both being relevant for high temperature plasmas. Thus, the spectrum KTAEs can be evaluated in realistic tokamak geometry.

The model enables the stability analysis of different scenarios including the tritium experiments at JET, where a large fraction of energetic particles is present, as well as the future fusion reactor experiments (ITER) with a significant fraction of alpha particles. The stability of small wave length Alfvén eigenmodes, relevant for the alpha particle confinement in a fusion reactor, can be analyzed using this method. The numerical procedure developed is appropriate to resolve the interaction between short wave length perturbations and energetic particles with complex orbit shapes.

The numerical evaluation of the power transfer δW_{hot} requires two main algorithms, namely for the integration of the particle orbits and for the phase-space integration. The orbit following algorithm uses 6 variables in order to handle the geometric singularity of the poloidal coordinates. Sufficient accuracy is achieved using around 100 Runga–Kutta fourth order steps per orbit. The scheme for the evaluation of the phase-space integration works accurately and efficiently. Convergence studies yield a scaling of the error consistent with a second order method in two dimensions. In the small orbit and large aspect ratio limit the results calculated by the CASTOR-K code agree well with those obtained from analytic theory [3]. Good numerical convergence is established, where an accuracy of 1% can be achieved with around 1000 evaluations of the integrand. In addition, the accuracy of the CASTOR-K code package also is assessed by benchmark tests with the FAC code and the NOVA-K code. These tests confirm in detail that the developed algorithms are robust and accurate. Furthermore, convergence studies show the new code can be applied to physical problems with sufficient efficiency.

The CASTOR-K code has been applied for detailed analysis of JET discharges during the DTE1 campaign [32, 16].

APPENDIX

A.1. *Particle Equations of Motion in CASTOR Curvilinear Coordinates*

The covariant and contra-variant components of CASTOR coordinates are

$$\mathbf{a}^1 = \nabla s, \tag{A.1.1}$$

$$\mathbf{a}_1 = J\nabla\tilde{\theta} \times \nabla\phi, \tag{A.1.2}$$

$$\mathbf{a}^2 = \nabla\tilde{\theta}, \tag{A.1.3}$$

$$\mathbf{a}_2 = J\nabla\phi \times \nabla s, \tag{A.1.4}$$

$$\mathbf{a}^3 = \nabla\phi, \tag{A.1.5}$$

$$\mathbf{a}_3 = J\nabla s \times \nabla\tilde{\theta}. \tag{A.1.6}$$

J is the Jacobian of the coordinate system $(s, \tilde{\theta}, \phi)$ and $f(s)\nabla s = \nabla\psi$. The metric coefficients are defined as

$$g^{11} = |\nabla s|^2, \tag{A.1.7}$$

$$g_{11} = \frac{J^2}{R^2}|\nabla\tilde{\theta}|^2, \tag{A.1.8}$$

$$g^{12} = \nabla s \cdot \nabla\tilde{\theta}, \tag{A.1.9}$$

$$g_{12} = -\frac{J^2}{R^2}\nabla s \cdot \nabla\tilde{\theta}, \tag{A.1.10}$$

$$g^{22} = |\nabla\tilde{\theta}|^2, \tag{A.1.11}$$

$$g_{22} = \frac{J^2}{R^2}|\nabla s|^2, \tag{A.1.12}$$

$$g^{23} = 0, \tag{A.1.13}$$

$$g_{23} = 0, \tag{A.1.14}$$

$$g^{33} = |\nabla\phi|^2 = \frac{1}{R^2}, \tag{A.1.15}$$

$$g_{33} = R^2, \tag{A.1.16}$$

where $R(s, \tilde{\theta})$ is the distance from the toroidal axis.

The differential operators required in the unperturbed orbit integrations are

$$\vec{k}_c = (\vec{b} \cdot \nabla)\vec{b}, \tag{A.1.17}$$

$$\vec{\Theta}_1 = \vec{b}, \tag{A.1.18}$$

$$\vec{\Theta}_3 = \vec{b} \times \nabla B, \tag{A.1.19}$$

$$\vec{\Theta}_2 = \vec{b} \times \vec{k}_c, \tag{A.1.20}$$

$$\Theta_4 = \vec{b} \cdot \nabla B, \tag{A.1.21}$$

$$\Theta_5 = \vec{b} \cdot \vec{k}_c = 0, \tag{A.1.22}$$

$$\Theta_6 = \vec{k}_c \cdot (\vec{b} \times \nabla B), \tag{A.1.23}$$

$$\Theta_7 = \vec{b} \cdot (\nabla \times \vec{b}), \tag{A.1.24}$$

where the contra-variant components of $\vec{k}_c$ and $\vec{w}$ are

$$k_c^1 = -\frac{g_{33}(-\partial b_1/\partial\theta + \partial b_2/\partial s)b_2 - (g_{12}(\partial b_3/\partial\theta) - g_{22}(\partial b_3/\partial s))b_3}{J(s,\tilde{\theta})^2}, \tag{A.1.25}$$

$$k_c^2 = \frac{(g_{33}(-(\partial b_1/\partial\theta) + \partial b_2/\partial s)b_1) - (g_{11}(\partial b_3/\partial\theta) - g_{12}(\partial b_3/\partial s))b_3}{J(s,\tilde{\theta})^2}, \tag{A.1.26}$$

$$k_c^3 = -\frac{(g_{12}(\partial b_3/\partial\theta) - g_{22}(\partial b_3/\partial s))b_1 - (g_{11}(\partial b_3/\partial\theta) - g_{12}(\partial b_3/\partial s))b_2}{J(s,\tilde{\theta})^2}, \tag{A.1.27}$$

$$w^1 = -\frac{(\partial B/\partial\tilde{\theta})b_3}{J(s,\tilde{\theta})}, \tag{A.1.28}$$

$$w^2 = \frac{(\partial B/\partial s)b_3}{J(s,\tilde{\theta})}, \tag{A.1.29}$$

$$w^3 = \frac{(\partial B/\partial\tilde{\theta})b_1 - (\partial B/\partial s)b_2}{J(s,\tilde{\theta})}, \tag{A.1.30}$$

where $\vec{w}$ is defined as

$$\vec{w} = \vec{b} \times \nabla B. \tag{A.1.31}$$

In the CASTOR curvilinear flux coordinates these operators take the form

$$\Theta_1^1 = g^{11}b_1 + g^{12}b_2 = b^1 = 0, \tag{A.1.32}$$

$$\Theta_1^2 = g^{12}b_1 + g^{22}b_2 = b^2 = \frac{f}{JB}, \tag{A.1.33}$$

$$\Theta_1^3 = g^{33}b_3, \tag{A.1.34}$$

$$\Theta_2^1 = \frac{g_{33}k_c^3b_2 - g_{12}k_c^1b_3 - g_{22}k_c^2b_3}{J(s,\tilde{\theta})}, \tag{A.1.35}$$

$$\Theta_2^2 = \frac{-g_{33}k_c^3b_1 + g_{11}k_c^1b_3 + g_{12}k_c^2b_3}{J(s,\tilde{\theta})}, \tag{A.1.36}$$

$$\Theta_2^3 = \frac{g_{12}k_c^1b_1 + g_{22}k_c^2b_1 - g_{11}k_c^1b_2 - g_{12}k_c^2b_2}{J(s,\tilde{\theta})}, \tag{A.1.37}$$

$$\Theta_3^1 = w^1, \tag{A.1.38}$$

$$\Theta_3^2 = w^2, \tag{A.1.39}$$

$$\Theta_3^3 = w^3, \tag{A.1.40}$$

$$\Theta_4 = \frac{\frac{\partial B}{\partial\theta}Fg_{33}}{q(s)B}, \tag{A.1.41}$$

$$\Theta_6 = g_{11}k_c^1w^1 + g_{12}k_c^2w^1 + g_{12}k_c^1w^2 + g_{22}k_c^2w^2 + g_{33}k_c^3w^3, \tag{A.1.42}$$

$$\Theta_7 = \frac{(\partial b_3/\partial\theta)b_1 - (\partial b_3/\partial s)b_2 + (-\partial b_1/\partial\theta + \partial b_2/\partial s)b_3}{J(s,\tilde{\theta})}. \tag{A.1.43}$$

A.2. *Discretization of the Orbit Integrals*

The implementation of the orbit integrals requires computation of the seven Θ factors present in the particle equations of motion numerically,

$$\left(1-\frac{1}{\Omega}v_\parallel\Theta_7\right)\dot{s} = v_\parallel\Theta_1^1 + \frac{v_\parallel^2}{\Omega}\left(\Theta_2^1+\Theta_1^1\Theta_7\right) + \frac{\mu}{m\Omega}\Theta_3^1, \tag{A.2.1}$$

$$\left(1-\frac{1}{\Omega}v_\parallel\Theta_7\right)\dot{\tilde{\theta}} = v_\parallel\Theta_1^2 + \frac{v_\parallel^2}{\Omega}\left(\Theta_2^2+\Theta_1^2\Theta_7\right) + \frac{\mu}{m\Omega}\Theta_3^2, \tag{A.2.2}$$

$$\left(1-\frac{1}{\Omega}v_\parallel\Theta_7\right)\dot{\phi} = v_\parallel\Theta_1^3 + \frac{v_\parallel^2}{\Omega}\left(\Theta_2^3+\Theta_1^3\Theta_7\right) + \frac{\mu}{m\Omega}\Theta_3^3, \tag{A.2.3}$$

$$\left(1-\frac{1}{\Omega}v_\parallel\Theta_7\right)\dot{v}_\parallel = -\frac{\mu}{m}\Theta_4 + \frac{\mu v_\parallel}{m\Omega}(\Theta_6-\Theta_4\Theta_7). \tag{A.2.4}$$

These equilibrium quantities Θ are functions of s (radius) and $\tilde{\theta}$ (generalized poloidal angle). An efficient two dimensional interpolation scheme is given by applying cubic splines in s and Fourier expansion with respect to the angle $\tilde{\theta}$. This interpolation must account for accurate representation of the equilibrium. In addition, all quantities must be consistent up to machine accuracy in order to ensure convergence of the orbit following procedure. Given an equilibrium reconstructed with the HELENA code, the splined equilibrium must be sufficiently close to the original magnetic configuration and, furthermore, operators like $\nabla\times\vec{b}$, ∇B, etc., must be represented accurate up to machine precision. The quantities required in the equations of motion are expressed in terms of f, F, q, b_1, b_2, and b_3 and their first derivatives in $s, \tilde{\theta}$. f, F, and q only depend on s, while b_1, b_2, and b_3 depend on s and $\tilde{\theta}$. The radial dependence is interpolated using cubic splines defined as

$$G_I(s,\tilde{\theta}) = \sum_j \left(aY_{n,j}+bY_{n+1,j}+(a^3-a)Y''_{n,j}+(b^3-b)Y''_{n+1,j}\right)\frac{h^2}{6}\sin(-j\tilde{\theta}), \tag{A.2.5}$$

$$G_P(s,\tilde{\theta}) = \sum_j \left(aY_{n,j}+bY_{n+1,j}+(a^3-a)Y''_{n,j}+(b^3-b)Y''_{n+1,j}\right)\frac{h^2}{6}\cos(-j\tilde{\theta}), \tag{A.2.6}$$

where

$$h = X_{n+1}-X_n, \tag{A.2.7}$$

$$a = \frac{X_{n+1}-x}{h}, \tag{A.2.8}$$

$$b = \frac{x-X_n}{h}. \tag{A.2.9}$$

Each array of splines contains the value of the function at each node and the corresponding second derivative in s. The Fourier decomposition uses the fact that all functions are either even or odd in $\tilde{\theta}$. Hence, the corresponding derivatives are represented as

$$\frac{\partial G_I(s,\tilde{\theta})}{\partial s} = \sum_j \left(daY_{n,j}+dbY_{n+1,j}+(3a^2-1)daY''_{n,j}\right.$$
$$\left.+(3b^2-1)dbY''_{n+1,j}\right)\frac{h^2}{6}(\sin(-j\tilde{\theta})), \tag{A.2.10}$$

$$\frac{\partial G_P(s,\tilde{\theta})}{\partial s} = \sum_j \big(daY_{n,j} + dbY_{n+1,j} + (3a^2-1)daY''_{n,j} + (3b^2-1)dbY''_{n+1,j}\big)\frac{h^2}{6}(\cos(-j\tilde{\theta})), \tag{A.2.11}$$

$$\frac{\partial G_I(s,\tilde{\theta})}{\partial \theta} = \sum_j \big(aY_{n,j} + bY_{n+1,j} + (a^3-a)Y''_{n,j} + (b^3-b)Y''_{n+1,j}\big)\frac{h^2}{6}(-j\cos(-j\tilde{\theta})), \tag{A.2.12}$$

$$\frac{\partial G_P(s,\tilde{\theta})}{\partial \theta} = \sum_j \big(aY_{n,j} + bY_{n+1,j} + (a^3-a)Y''_{n,j} + (b^3-b)Y''_{n+1,j}\big)\frac{h^2}{6}(j\sin(-j\tilde{\theta})), \tag{A.2.13}$$

where $da = -\frac{1}{h}$ and $db = \frac{1}{h}$.

It is easy to see that b_1, $\partial b_1/\partial s$, $\partial b_2/\partial\tilde{\theta}$, and $\partial b_3/\partial\tilde{\theta}$ are odd functions in $\tilde{\theta}$ and $\partial b_1/\partial\tilde{\theta}$, $\partial b_2/\partial s$, $\partial b_3/\partial s$, b_2, and b_3 are even functions in $\tilde{\theta}$. Defining B and its derivatives

$$B = \frac{F}{b_3}, \tag{A.2.14}$$

$$\frac{\partial B}{\partial s} = \frac{(\partial F/\partial s)b_3 - F(\partial b_3/\partial s)}{b_3^2}, \tag{A.2.15}$$

$$\frac{\partial B}{\partial \tilde{\theta}} = -\frac{F(\partial b_3/\partial\tilde{\theta})}{b_3^2}, \tag{A.2.16}$$

the Θ terms can now be represented using splines. The following expressions represent the metric coefficients in the new representation

$$g_{11} = \frac{f^2q + F^2qb_1^2 + BFb_1^2b_2}{BFb_2}, \tag{A.2.17}$$

$$g_{12} = \frac{b_1(Fq + Bb_2)}{B}, \tag{A.2.18}$$

$$g_{22} = \frac{Fqb_2}{B} + b_2^2, \tag{A.2.19}$$

$$g_{33} = \frac{F(Fq + Bb_2)}{B^2q}, \tag{A.2.20}$$

$$g^{11} = \frac{BFb_2}{f^2q}, \tag{A.2.21}$$

$$g^{12} = -\frac{BFb_1}{f^2q}, \tag{A.2.22}$$

$$g^{22} = \frac{BFb_1^2}{f^2qb_2} + \frac{B}{Fqb_2 + Bb_2^2}, \tag{A.2.23}$$

$$g^{33} = \frac{B^2q}{F^2q + BFb_2}. \tag{A.2.24}$$

Finally the Θ terms are

$$\Theta_1^1 = 0, \tag{A.2.25}$$

$$\Theta_1^2 = \frac{B}{Fq + Bb_2}, \tag{A.2.26}$$

$$\Theta_1^3 = \frac{B^2 q b_3}{F^2 q + BFb_2}, \tag{A.2.27}$$

$$\Theta_2^1 = -\frac{B^3(\partial b_3/\partial\tilde{\theta})\left(Fb_2 + Bqb_3^2\right)}{fF(Fq + Bb_2)^2}, \tag{A.2.28}$$

$$\Theta_2^2 = \frac{B^3\left(\left(\partial b_3/\partial\tilde{\theta}\right)Fb_1 - (\partial b_1/\partial\tilde{\theta})Fb_3 + (\partial b_2/\partial s)Fb_3 + B(\partial b_3/\partial s)qb_3^2\right)}{fF(Fq + Bb_2)^2}, \tag{A.2.29}$$

$$\Theta_2^3 = \frac{B^3((\partial b_1/\partial\tilde{\theta})Fb_2 - (\partial b_2/\partial s)Fb_2 + B(\partial b_3/\partial\tilde{\theta})qb_1b_3 - B(\partial b_3/\partial s)qb_2b_3)}{fF(Fq + Bb_2)^2}, \tag{A.2.30}$$

$$\Theta_3^1 = -\frac{B^2(\partial B/\partial\tilde{\theta})b_3}{f(Fq + Bb_2)}, \tag{A.2.31}$$

$$\Theta_3^2 = \frac{B^2(\partial B/\partial s)b_3}{f(Fq + Bb_2)}, \tag{A.2.32}$$

$$\Theta_3^3 = \frac{B^2((\partial B/\partial\tilde{\theta})b_1 - (\partial B/\partial s)b_2)}{f(Fq + Bb_2)}, \tag{A.2.33}$$

$$\Theta_4 = \frac{B(\partial B/\partial\tilde{\theta})}{Fq + Bb_2}, \tag{A.2.34}$$

$$\Theta_6 = \frac{B^3(-((\partial B/\partial\tilde{\theta})(\partial b_3/\partial\tilde{\theta})Fb_1) + (\partial B/\partial s)(\partial b_3/\partial\tilde{\theta})Fb_2 + (\partial B/\partial\tilde{\theta})(\partial b_1/\partial\tilde{\theta})Fb_3 - (\partial B/\partial\tilde{\theta})(\partial b_2/\partial s)Fb_3)}{fF(Fq + Bb_2)^2}$$
$$+ B^3\left(\frac{B(\partial B/\partial s)(\partial b_3/\partial\tilde{\theta})qb_3^2 - B(\partial B/\partial\tilde{\theta})(\partial b_3/\partial s)qb_3^2}{fF(Fq + Bb_2)^2}\right), \tag{A.2.35}$$

$$\Theta_7 = \frac{B^2((\partial b_3/\partial\tilde{\theta})b_1 - (\partial b_3/\partial s)b_2 - (\partial b_1/\partial\tilde{\theta})b_3 + (\partial b_2/\partial s)b_3)}{f(Fq + Bb_2)}. \tag{A.2.36}$$

A.3. *Accuracy of the Magnetic Field Representation*

It is essential that the orbit integrals are performed sufficiently accurately; here the accuracy depends crucially on the representation of the magnetic field. The radial coordinate dependence is represented by cubic finite elements, and the dependence on the poloidal coordinate by a Fourier decomposition. The choice made for the representation of the functions b_1, b_2, b_3 guarantees that the field is consistent, i.e., $\nabla \cdot \vec{B} = 0$ (up to machine accuracy $e_r \approx 10^{-15}$) and that all the differential operators required in the orbit integrals are represented up to machine precision. This fact is confirmed by the level of accuracy by which the invariants of motion are conserved during the orbit integrations (III.4). Independent of the number of radial nodes used, and of the number of Fourier modes, the particle orbits are well described by the field representation. Depending on the equilibrium configuration

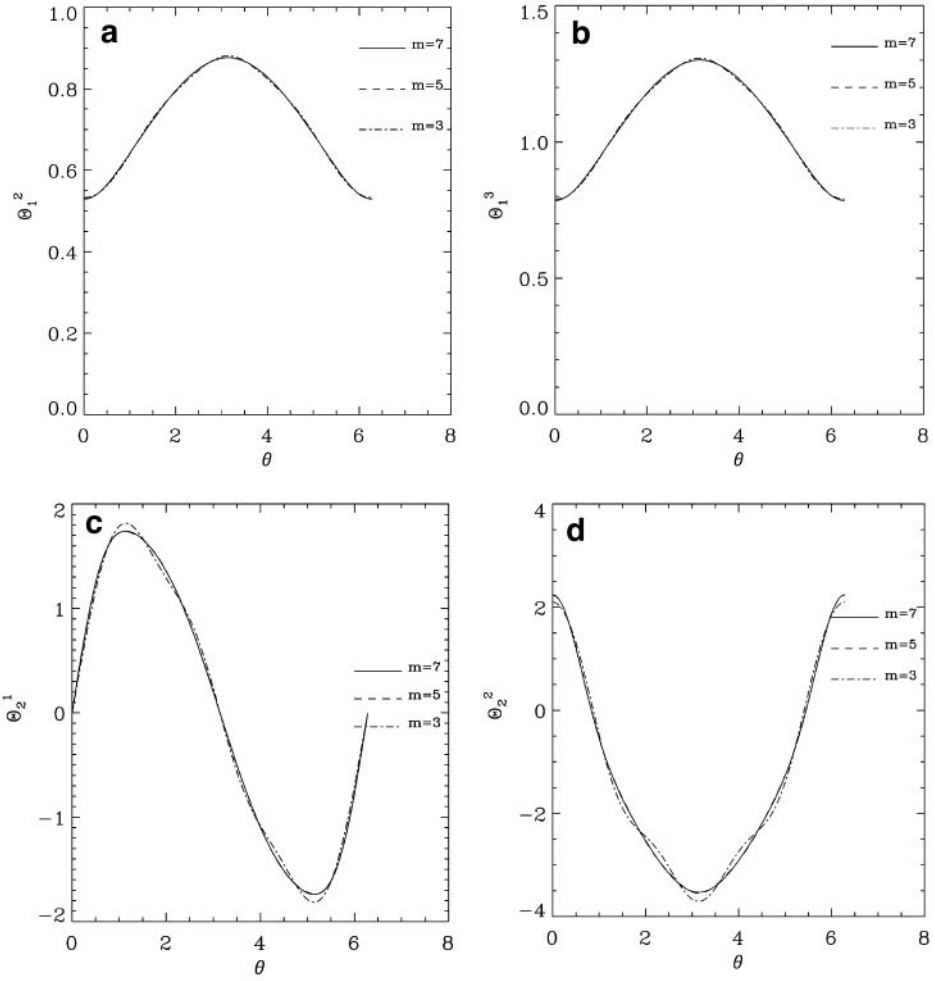

FIG. A.3. (a) Representation of Θ_1^2 using 3, 5, and 7 poloidal harmonics. (b) Representation of Θ_1^3 using 3, 5, and 7 poloidal harmonics. (c) Representation of Θ_2^1 using 3, 5, and 7 poloidal harmonics. (d) Representation of Θ_2^2 using 3, 5, and 7 poloidal harmonics. (e) Representation of Θ_2^3 using 3, 5, and 7 poloidal harmonics. (f) Representation of Θ_3^3 using 3, 5, and 7 poloidal harmonics. (g) Representation of Θ_6 using 3, 5, and 7 poloidal harmonics. (h) Representation of Θ_7 using 3, 5, and 7 poloidal harmonics.

the resolution required in the field representation can change; simple circular cross-section equilibria require only a few poloidal harmonics, while strongly shaped triangular plasmas require more than 5 Fourier components. For plasmas, where the plasma boundary is determined by a separatrix, the coordinates used in CASTOR cannot represent the last closed flux surfaces accurately. The functions that represent the magnetic field near the separatrix have a strong dependence in $\tilde{\theta}$ close to the X-point and require a large number of Fourier harmonics for accurate representation. The analysis of the excitation of global modes by energetic ions does not require the inclusion of kinetic effects at the plasma boundary, since the plasma edge is dominated by low temperatures and the density of energetic ions is very small. For this reason a less accurate representation of the plasma boundary does not constitute a problem. The number of radial cubic elements and poloidal Fourier components used

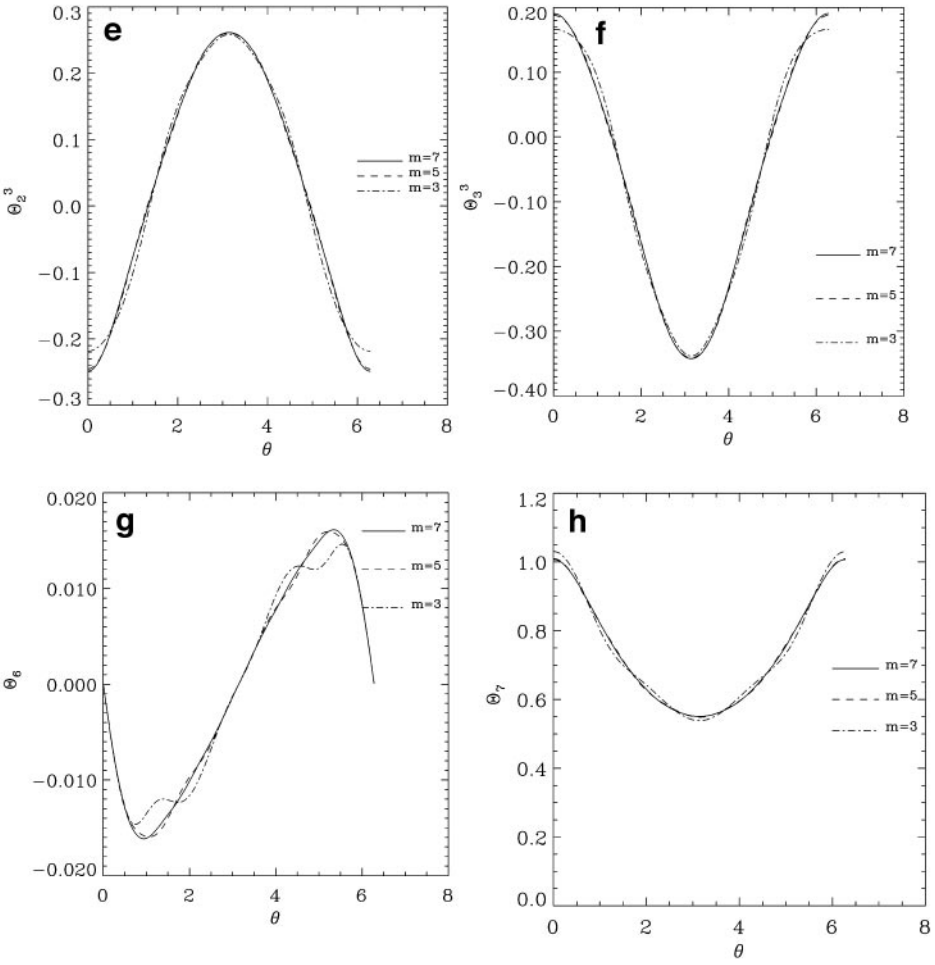

FIG. A.3—*Continued*

depend on the accuracy required in the representation of the equilibrium. As 1% accuracy is sufficient in most applications, 41 radial grid points and 7 Fourier components are used.

For a JET equilibrium the functions which are more difficult to represent are Θ_6 and Θ_7 as defined in Appendix 2. The functions Θ_1^1, Θ_1^2, Θ_1^3, Θ_2^1, Θ_2^2, Θ_2^3, Θ_3^3, and Θ_4 can be represented accurately with 5 poloidal harmonics in the region $s \in [0, 0.8]$, while Θ_6 and Θ_7 require 7 poloidal harmonics. The results shown in Figs. A.3a–A.3f give evidence of the high accuracy achieved with only 5 harmonics for the quantities Θ_1^1, Θ_1^2, Θ_1^3, Θ_2^1, Θ_2^2, Θ_2^3, Θ_3^3, and Θ_4; only the quantities Θ_6 and Θ_7 require 7 poloidal harmonics for the same level of accuracy as shown in Figs. A.3g–A.3h.

ACKNOWLEDGMENTS

We thank Dr. G. Fu for the possibility of benchmarking the CASTOR-K code with the NOVA-K code and Dr. J. Candy for the benchmark with the FAC code and for stimulating and useful discusions.

REFERENCES

1. M. Abramowitz and A. Stegun, *Handbook of Mathematical Functions* (Dover, New York, 1965).
2. H. L. Berk, J. W. Van Dam, D. Borba, J. Candy, G. T. A. Huysmans, and S. Sharapov, More on core localized toroidal Alfvén eigenmodes, *Phys. Plasmas* **2**(9), 3401 (1995).
3. R. Betti and J. P. Freidberg, A stability criterion for energetic particle Alfvén modes. *Phys. Fluids B* **3**(3), 538 (1991).
4. S. Briguglio, G. Vlad, F. Zonca, and C. Kar, Hybrid magnetohydrodynamic-gyrokinetic simulation of toroidal Alfvén modes, *Phys. Plasmas* **2**(10), 3711 (1995).
5. J. Candy, D. Borba, H. L. Berk, G. T. A. Huysmans, and W. Kerner, Nonlinear interaction of fast particles with Alfvén waves in toroidal plasmas, *Phys. Plasmas* **4**(7), 2597 (1997).
6. Liu Chen, R. B. White, and M. N. Rosenbluth, Excitation of internal kink modes by trapped energetic beam ions, *Phys. Rev. Lett.* **52**(13), 1122 (1984).
7. C. Z. Cheng and M. S. Chance, Low-n shear Alfvén spectra in axisymmetric toroidal plasmas, *Phys. Fluids* **29**(11), 3695 (1986).
8. C. Z. Cheng, Energetic particle effects on global magnetohydrodynamics modes, *Phys. Fluids B* **2**(6), 1427 (1990).
9. C. Z. Cheng, Alpha particle destabilization of the toroidicity-induced Alfvén eigenmodes, *Phys. Fluids B* **3**(9), 2463 (1991).
10. M. S. Chu, J. M. Green, L. L. Lao, A. D. Turnbull, and M. S. Chance, A numerical study of the high-n shear Alfvén spectrum gap and the high-n gap mode, *Phys. Fluids B* **4**(11), 3713 (1992).
11. J. W. Connor, R. O. Denny, R. J. Hastie, D. Borba, G. T. A. Huysmans, W. Kerner, and S. Sharapov, Nonideal effects on toroidal Alfvén eigenmode stability, in *Proceedings, European Plasma Physics Conference 1994*, Vol. 18 B, Part II, p. 616.
12. B. Coppi, S. Migliuolo, and F. Porcelli, Macroscopic plasma oscillation bursts (fishbones) resulting from high energy populations, *Phys. Fluids* **31**(6), 1630 (1988).
13. B. Coppi, S. Migliuolo, F. Pegoraro, and F. Porcelli, Global modes and high-energy particles in ignited plasmas, *Phys. Fluids B* **2**(5), 927 (1990).
14. A. Fasoli, J. B. Lister, S. Sharapov, S. Ali-Arshad, G. Bosia, D. Borba, D. J. Campbell, N. Deliyanakis, J. A. Dobbing, C. Gormezano, J. Jacquinot, A. Jaun, H. A. Holties, G. T. A. Huysmans, W. Kerner, P. Lavanchy, J. M. Moret, L. Porte A. Santagiustina, and L. Villard, Overview of Alfvén eigenmode experiments in JET, *Nucl. Fusion* **35**(12), 1485 (1995).
15. A. Fasoli, J. B. Lister, S. Sharapov, D. Borba, N. Deliyanakis, C. Gormezano, J. Jacquinot, A. Jaun, H. A. Holties, G. T. A. Huysmans, W. Kerner, J. M. Moret, and L. Villard, Observation of multiple kinetic Alfvén eigenmodes, *Phys. Rev. Lett.* **76**(7), 1097 (1996).
16. A. Fasoli, D. Borba, C. Gormezano, R. Heeter, A. Jaun, J. Jacquinot, W. Kerner, Q. King, J. B. Lister, S. Sharapov, D. Start, and L. Villard, Alfvén eigenmode experiments in tokamaks and stellarators, *Plasma Phys. Control. Fusion* **39**(12B), (1997).
17. G. Y. Fu and J. W. Van Dam, Excitation of the toriodicity-induced shear Alfvén eigenmode by fusion alpha particles in an ignited tokamak, *Phys. Fluids B* **1**(10), 1949 (1989).
18. G. Y. Fu and J. W. Van Dam, Stability of the global Alfvén eigenmode in the presence of fusion alpha particles in an ignited tokamak plasma, *Phys. Fluids B* **1**(12), 2404 (1989).
19. G. Y. Fu and C. Z. Cheng, Excitation of high-n toroidicity-induced shear Alvfén eigenmodes by energetic particles and fusion alpha particles in tokamaks, *Phys. Fluids B* **4**(11), 3722 (1992).
20. G. Y. Fu, C. Z. Cheng, and K. L. Wong, Stability of the toroidicity-induced Alfvén eigenmodes in axisymmetric toroidal equilibria, *Phys. Fluids B* **5**(11), 4040 (1993).
21. G. Y. Fu, Existence of core localized toroidicity-induced Alfvén eigenmode, *Phys. Plasmas* **2**(4), 1029 (1995).
22. N. N. Gorelenkov and S. E. Sharapov, On the collisional damping of TAE modes on trapped electrons in tokamaks, *Phys. Scr.* **45**, 163 (1991).
23. W. W. Heidbrink and G. Sager, The Fishbone instability in the DIII-D tokamak, *Nucl. Fusion* **30**(6), 1015 (1990).

24. C. T. Hsu and D. J. Sigmar, Alpha-particle losses from toroidicity-induced Alfvén eigenmodes. Part I. Phase-space topology of energetic particle orbits in tokamak plasma, *Phys. Fluids B* **4**(6), 1493 (1992).
25. C. T. Hsu and D. J. Sigmar, Alpha-particle losses from toroidicity-induced Alfvén eigenmodes: Monte Carlo simulations and anomalous alpha-loss process, *Phys. Fluids B* **3**(6), 1506 (1992).
26. G. T. A. Huysmans, J. P. Goedbloed, and W. Kerner, External resistive modes in tokamaks, *Phys. Fluids B* **5**, 1545 (1993).
27. G. T. A. Huysmans, H. A. Holties, J. P. Goedbloed, W. Kerner, and D. Borba, Modelling the excitation of global Alfvén modes by an external antenna in JET, *Phys. Plasmas* **2**(5), 1605 (1995).
28. T. Kass, H. S. Bosch, H. U. Fahrbach, W. Herrmann, F. Hoenen, M. Maraschek, and H. Zohm, Investigation of the fishbone instability in ASDEX upgrade, in *22nd EPS on Plasma Physics and Controlled Fusion, Bournemouth 1995*, Part IV, p. 41.
29. W. Kerner, Large-scale complex eigenvalue problems, *J. Comput. Phys.* **85**(1), 1 (1989).
30. W. Kerner, D. Borba, G. T. A. Huysmans, F. Porcelli, S. Poedts, J. P. Goedbloed, and R. Betti, Stability of global Alfvén waves (TAE, EAE) in JET tritium discharges, *Plasma Phys. Control. Fusion* **36**, 911 (1994).
31. W. Kerner, J. P. Goedbloed, G. T. A. Huysmans, S. Poedts, and E. Schwarz, CASTOR: Normal-mode analysis of resistive MHD plasmas, *J. Comput. Phys.* **142**, 271 (1998).
32. W. Kerner, D. Borba, S. E. Sharapov, B. N. Breizman, J. Candy, A. Fasoli, L. C. Appel, R. Heeter, L.-G. Eriksson, and M. Mantsinen, Theory of Alfvén eigenmode instabilities and related alpha particle transport in JET deuterium-tritium plasmas, *Nucl. Fusion* **38**(9), 1315 (1998).
33. R. G. Littlejohn, Variational principles of guiding centre motion, *J. Plasma Phys.* **29**, 111 (1983).
34. K. McGuire, R. Goldston, M. Bell, M. Bitter, K. Bol, K. Brau, D. Buchenauer, T. Crowley, S. Davis, F. Dylla, H. Eubank, H. Fishman, R. Fonck, B. Grek, R. Grimm, R. Hawryluk, H. Hsan, R. Hulse, R. Izzo, R. Kaita, S. Kaye, H. Kugel, D. Johnson, J. Manickam, D. Manos, D. Mansfield, E. Mazzucato, R. McCann, D. McCune, D. Monticello, R. Motley, D, Mueller, K. Oasa, M. Okabayashi, K. Owens, W. Park, M. Reusch, N. Sauthoff, G. Schmidt, S. Sesnic, J. Strachan, C. Surko, R. Slusher, H. Takahashi, F. Tenney, P. Thomas, H. Towner, J. Valley, and R. White, Study of high-beta magnetohydrodynamic modes and fast ion losses in PDX, *Phys. Phys. Rev. Lett.* **50**, 891 (1983).
35. R. R. Mett and S. M. Mahajan, Kinetic theory of toriodicity-induced Alfvén eigenmodes, *Phys. Fluids B* **4**(9), 2885 (1992).
36. R. R. Mett, E. J. Strait, and S. M. Mahajan, Damping of toroidal Alfvén modes in DIII-D, *Phys. Plasmas* **1**(10), 3277 (1994).
37. A. B. Mikhailovskii, "Drift" excitation of Alfvén waves by trapped electrons in a tokamak with $\beta_j > 1$, *Sov. J. Plasma Phys.* **3**, 207 (1975).
38. M. F. F. Nave, D. J. Campbell, E. Joffrin, F. B. Marcus, G. Sadler, P. Smeulders, and K. Thomsen, Fishbone activity in JET, *Nucl. Fusion* **31**(4), 697 (1991).
39. M. F. F. Nave, S. Ali-Arshad, B. Alper, B. Balet, D. Borba, C. D. Challis, H. J. de Blank, M. von Hellermann, T. C. Hender, G. T. A. Huysmans, W. Kerner, G. Kramer, F. Porcelli, J. O. Rourke, L. Porte, G. Sadler, P. Smeulders, A. C. C. Sips, P. M. Stubberfield, D. Stork, R. Reichle, J. Wesson, and W. Zwingmann, MHD activity in JET hot ion H-Mode discharges, *Nucl. Fusion* **35**(4), (1995).
40. S. Poedts and E. Schwartz, Computation of the ideal MHD continuous spectrum in axisymmetric plasmas, *J. Comput. Phys.* **105**(1), 165 (1993).
41. F. Porcelli, R. Stankiewicz, H. L. Berk, and Y. Z. Zhang, Internal kink stabilization by high-energy ions with nonstandard orbits, *Phys. Fluids B* **4**(10), 3017 (1992).
42. F. Porcelli, W. Kerner, R. Stankiewicz, and H. L. Berk, Solution of the drift-kinetic equation for global plasma modes and finite particle orbit widths, *Phys. Plasmas* **1**(3), 470 (1994).
43. F. Porcelli, L.-G. Eriksson, and I. Furno, Topological transitions of fast ion orbits in magnetically confined plasmas, *Phys. Lett. A* **216**(6), 289 (1996).
44. M. N. Rosenbluth and P. H. Rutherford, Excitation of Alfvén waves by high energy ions in a tokamak, *Phys. Rev. Lett.* **34**(23), 1429 (1975).
45. R. A. Santoro and Liu Chen, Gyrokinetic-magnetohydrodynamic hydrid simulation of the transition from toroidal Alfvén eigenmodes to kinetic ballooning modes in tokamaks, *Phys. Plasmas* **3**(6), 2349 (1996).

46. R. B. White and M. S. Chance, Hamiltonian guiding center drift orbit calculation for plasmas of arbitrary cross section, *Phys. Fluids* **27**(10), 2455 (1984).
47. R. B. White, F. Romanelli, and M. N. Bussac, Influence of an energetic ion population on tokamak plasma stability, *Phys. Fluids B* **2**(4), 745 (1990).
48. R. B. White, E. Fredrickson, D. Darrow, M. Zamstorff, R. Wilson, S. Zweben, K. Hill, Y. Chen, and G. Fu, Toroidal Alfvén eigenmode-induced ripple trapping, *Phys. Plasmas* **2**(8), 2871 (1995).
49. H. V. Wong, H. L. Berk, and B. N. Breizman, Orbit width scaling of TAE instability growth rate, *Nucl. Fusion* **35**(12), 1721 (1995).
50. K. L. Wong, R. J. Fonck, S. F. Paul, D. R. Roberts, E. D. Fredrickson, R. Nazikian, H. K. Park, M. Bell, N. L. Bretz, Budny, S. Cohen, G. W. Hammett, F. C. Jobes, D. M. Meade, S. S. Medley, D. Mueller, Y. Nagayama, D. K. Owens, and E. J. Synakowski, Excitation of toroidal Alfvén eigenmodes in TFTR, *Phys. Rev. Lett.* **66**(14), 1876 (1991).
51. N. I. Grishanov, C. A. de Azevedo, and A. S. de Assis, Longitudinal permittivity of a tokamak plasma with elliptic and circular magnetic surfaces, *Phys. Plasmas* **5**(3), 705 (1998).
52. N. N. Gorelenkov, C. Z. Cheng, Y. Chen, G. Y. Fu, R. Nazikian, and R. B. White, Linear and nonlinear study of fast particle excitation of Alfvén eigenmodes, in *Proceedings, 17th IAEA Fusion Energy Conference Yokohama, 1998* (International Atomic Energy Agency, Vienna, 1999), IAEA-CN- 69/THP2-21-98.